Numerical Simulation of the Wave Bottom Boundary Layer Over a Smooth Surface. Part 1: Three-Dimensional Simulations.

Stéphanie S. Moneris and Donald N. Slinn

Submitted to the
Journal of Geophysical Research - Oceans

University of Florida

Gainesville, Florida

June, 2002

Abstract

Shoaling surface waves create turbulent shear flows at the sea-bed and thereby contribute to wave energy dissipation in the bottom boundary layer. Oscillatory boundary layers are examined using a high-resolution time-dependent three-dimensional numerical model. Near-bed free-stream velocities, similar to those common in nature, have been applied. The model makes direct estimates for wave energy dissipation rates and turbulent kinetic energy levels for turbulent boundary layers that occur over a smooth bottom. Results indicate that turbulence levels are coupled to the wave cycle; phases of accelerating flow organize the boundary layer structure, decelerating flow destabilizes it, and flow reversal induces the strongest turbulent bursts. Details of the flow (boundary layer thickness, turbulent kinetic energy, kinetic energy dissipation rate, velocity profiles, bed shear stress) are function of the Reynolds number, wave frequency, wave complexity, presence of a mean current, and the preceding flow history. Numerical experiments simulate the different flow regimes, laminar, transitional, and turbulent, that are produced.

1 Introduction

Turbulent boundary layers are a complex and important phenomena arising in oceanic fluid dynamics. For example, the high turbulence levels and shear stresses produced by surface waves are believed to play an important role in determining the suspension and transport of sediment. Shoaling surface waves create turbulent shear flows in the boundary layer at the sea floor and can thereby make significant contributions to wave energetics and dissipation rates. *Mei* [1989] has shown that the wave bottom boundary layer can make the dominant contribution to wave energy dissipation rates on broad shallow shelves in regions where active surface wave breaking does not occur.

Previous studies of wave-induced flows have focused on determining the bottom friction [*Bijker*, 1966; *Johns*, 1977; *Liu and Dalrymple*, 1978; *Grant et al.*, 1984; *Asano et al.*, 1986; *Huntley and Hazen*, 1988; *O'Connor and Yoo*, 1988; *Myrhaug and Slaattelid*, 1990; *Sleath*, 1991; *Soulsby et al.*, 1993; *Zhao and Anastasiou*, 1993; *Feddersen and Guza*, 2000; and *Rankin and Hires*, 2000]; others have investigated wave flows over rough beds [*Myrhaug*, 1982; *Trowbridge and Madsen*, 1984; *Sleath*, 1987, 1988; *Justesen*, 1988; *Lambrakos et al.*, 1988; *Garcez Faria et al.*, 1998; *Li and Amos*, 1998; *Fredsoe et al.*, 1999; *Houwman and Van Rijn*, 1999; *Mathisen and Madsen*, 1999; and *Barrantes and Madsen*, 2000]; while some have focused attention on sediment transport due to wave motion [*Bakker and Van Doorn*, 1978a; *Hanes and Huntley*, 1986; *Dyer and Soulsby*, 1988; *Hanes*, 1988; *Dick et al.*, 1994; *Foster et al.*, 1994; *Hay and Bowen*, 1994; *Ribberink and Al-Salem*, 1994; *Staub et al.*, 1996; and *Davies et al.*, 1997]. The purpose of the present work is to study turbulent kinetic energy and dissipation rates in a turbulent wave bottom boundary layer using numerical simulations.

The wave bottom boundary layer (WBBL) is highly unsteady and exhibits different types of behavior at different phases of the wave period, that can be significantly different

from flow observed in steady, uni-directional boundary layers. For example, the oscillatory boundary layer produces the phenomenon of overshoot near the bed [*Nielsen*, 1992] where the maximum current in the boundary layer during periods of flow acceleration is larger than the free stream velocity. Another significant characteristic is that wave phases of decelerations can destabilize the boundary layer and induce an inflectional instability at flow reversal, while accelerations tend to organize the boundary layer structure. For different wave field conditions and water depths the wave bottom boundary layer can be either laminar or turbulent. Ranges for laminar, transitioning, and turbulent flows, based on the amplitude or frequency Reynolds number, $Re_{A_m} = \frac{U_m A_m}{\nu} = Re_\omega = \frac{A_m^2 \omega}{\nu}$ have been determined. Here U_m is the maximum free stream velocity amplitude, A_m the free-stream particle amplitude or excursion length, such that $A_m = U_m/\omega$, ω the wave frequency, and ν the kinematic viscosity. The transition from laminar to turbulent flow has been found to take place over a smooth bottom for the amplitude Reynolds number in the interval $2\text{x}10^5 < Re_{A_m} < 6\text{x}10^5$. *Jonsson* [1980] found transition to occur near $Re_{A_m} = 10^5$. Laboratory experiments [*Kamphuis*, 1975; *Sleath*, 1987; *Hino et al.*, 1989; and *Jensen et al.*, 1989] have examined the variation in friction factor, $f_\omega = 2\tau_{wmax}/\rho U_m^2$, as a function of the Reynolds number, where τ_{wmax} is the maximum shear at the wall and ρ the fluid density.

The wave bottom boundary layer has been studied extensively, using laboratory observations, field experiments, and numerical computations. Several laboratory observations related to the wave bottom boundary layer over smooth boundaries have been performed. *Gad-El-Hak et al.* [1984] investigated the stability of decelerating boundary-layer flows. The boundary layer becomes unstable to two-dimensional waves, which become three-dimensional, generating hairpin vortices and turbulent bursts. *Sarpkaya* [1993] investigated the creation and development of low-speed streaks and coherent structures (e.g., arches, hairpins) on a long cylindrical body immersed in an oscillating flow.

Flow instability depended on strong pressure gradients, inflection points in velocity profiles and shear stress reversals. The transitional and turbulent states depend on the Reynolds number based on the boundary layer thickness, δ, $Re_\delta = U_m\delta/\nu$, and develop vortical motions which burst during periods of decelerating flows.

The first field observations of the wave bottom oscillatory boundary layer were presented by *Trowbridge and Agraval* [1995]. The measurements obtained indicate a distortion in the mean alongshore velocity in the boundary layer, a reduction in amplitude, and an increase in phase in comparison to the velocity in the outer region. *Foster et al.* [2000] present field measurements of the wave bottom boundary layer cross-shore velocity within the surf zone under strongly nonlinear wave forms. These observations are among the first coherent looks at the wave bottom boundary layer in the nearshore region.

Spalart [1987] and *Spalart and Baldwin* [1987] were first to develop a three-dimensional Navier-Stokes solver for the direct numerical simulations of an oscillatory turbulent boundary layer. Their model used a spectral method in a semi-infinite domain, perpendicular to the boundary and two periodic directions horizontally. The oscillating boundary layer flow displayed complex behavior, a function of the phase angle, ωt, and the Reynolds number, $Re_{\delta_s} = U_m\delta_s/\nu$, where $\delta_s = U_m\sqrt{\dfrac{2}{\nu\omega}}$ is the Stokes boundary layer thickness. *Akhavan et al.* [1991] investigated the stability of an oscillatory flow to different small disturbances by direct numerical simulations of the Navier-Stokes equations using spectral techniques. They concluded that transition to turbulence in oscillatory Stokes layers can be explained by a secondary instability mechanism of two-dimensional finite-amplitude waves to a three-dimensional infinitesimal instability mechanism. They found a transitional Reynolds number of the order of $Re_{\delta_s} \sim 500$. *Yang et al.* [1992] investigated by direct numerical simulation the laminar-turbulent transition in a decelerating flat-plate boundary layer. They observed two dimensional waves in the early

stages of transition. Comparisons to the experiments done by *Gad-El-Hak et al.* [1984] show good agreement. *Vittori and Verzicco* [1998] recently performed three-dimensional numerical simulations of the Stokes boundary layer over a wall with small roughness imperfections to analyze the influence on transition from the laminar to turbulent flow. Comparisons to analytical [*Blondeaux*, 1990] and experimental [*Jensen et al.*, 1989] results were in reasonable agreement. *Piomelli et al.* [2000] studied vortical structures in spatially developing turbulent boundary layers subjected to flow acceleration in two cases, low and strong accelerations. In the mild-acceleration case, an equilibrium of the boundary layer is obtained. The structure of turbulence is modified, longer streaks and fewer coherent vortices are observed. In strongly accelerating cases, the flow tends to approach the laminar profile. In both cases, the turbulent kinetic energy increases less rapidly than the energy of the mean flow.

Accurate knowledge of the combined wave-current motion is vital for wave forecasting and sediment transport, the sediment being usually suspended into the water column by the waves and transported by the current. *Lundgren* [1972] divided the flow depth in the combined wave-current motion into roughly three zones. In the upper zone, the turbulence is purely associated with the mean current and the turbulent characteristics are independent of the waves. In the transition zone, the turbulent motions produced by the wave boundary layer are of the same order of magnitude as those supported by instabilities of the mean current. The lower zone is dominated by wave-produced turbulence.

Wave-current flows have also been investigated theoretically and experimentally. *Lundgren* [1972] determined a theory for the combined wave-current motion using the eddy-viscosity concept. This model is a time-averaged model which does not take into account the variations with time of the boundary layer. A simplified model based on Lundgren's ideas was later developed by *Fredsoe* [1984] who considered both the case of

a pure oscillating wave boundary layer, assuming the velocity profile near the wall to be logarithmic, and the combined wave-current motion. *Grant and Madsen* [1979, 1986] have developed, using the eddy viscosity concept, a more detailed model for combined wave-current flow than that of Lundgren. In this approach, the eddy viscosity and the boundary layer thickness are assumed to be constant in time and all variations with time are assumed to be sinusoidal. The addition of a wave on the steady current above the wave boundary layer results in an increase in the apparent roughness experienced by the current. The eddy viscosity model proposed by Grant and Madsen focuses on the case of a steady current interacting with monochromatic waves over a rough bottom. They noticed that current above the wave boundary layer experiences a larger resistance due to the presence of waves than in the pure current flow. In the case of a pure oscillatory wave, the predictions of the velocity magnitude give good agreements with experimental results of *Jonsson and Carlsen* [1976] however the phase of the velocity is not so well predicted. *Smith* [1977] has taken a similar approach, his model treats only the co-directional flow cases and assumes that the problem of interest is the interaction of waves and currents in a current-dominated environment, whereas Grant and Madsen approach the problem from the opposite end. *Asano and Iwagaki* [1984] present a mathematical model based on Grant and Madsen's model to calculate velocities in wave-current co-existing flows. Measurements have also been performed and comparisons of the calculated results and experimental data show reasonable agreement. Their experiments showed a reduction of the current strength due to the presence of waves. *Myrhaug and Slaattelid* [1989] developed a theoretical model describing the motion in combined wave and current boundary layers near fixed rough sea-beds. A three-layer time invariant eddy viscosity model was employed. The combined flow demonstrates a clear reduction in the steady component of the velocity near the sea-bed compared with the no waves situation. *Christoffersen and Jonsson* [1985] used two simple two-layer linearly varying eddy-viscosity models. These

models have the same viscosities in the current boundary layer but different viscosities in the wave boundary layer. Other studies of the wave-current interactions were performed by *Coffey and Nielsen* [1984, 1986], *Davies et al.* [1988], among others.

Bakker and Van Doorn [1978b] applied mixing length theory and included in their mathematical model the time variation in the eddy viscosity. The assumption of a mixing length hypothesis, however, in a strongly unsteady flow is questionable. *Van Kesteren and Bakker* [1984] also determined the bottom friction due to a wave-current flow using the Prandtl hypothesis. Results obtained are less accurate than the ones found by *Lundgren* [1972] and *Bakker and Van Doorn* [1978b] due to Prandtl theory deficiencies.

Most of the existing theoretical models, e.g., *Grant and Madsen* [1979, 1986], *Myrhaug and Slaattelid* [1989], and *Christoffersen and Jonsson* [1985] suggest that the addition of a current to a wave boundary layer will increase the turbulence intensity and the eddy viscosity in the bottom boundary layer. The experimental data, however, indicate that the effect is weaker than the models have predicted. Measurements from *Van Doorn* [1981], *Kemp and Simons* [1982, 1983], and *Sleath* [1990] show that the influence of a mean current over a wave flow depends on the intensity of the mean current.

Our paper is organized as follows; first, the high-resolution three-dimensional time-dependent numerical model of the wave bottom boundary layer is reviewed in Section 2. Results obtained with the three-dimensional model with different wave forcing conditions are analyzed in Section 3. A summary is presented in Section 4. Comparisons between the three-dimensional model results and one-dimensional eddy-viscosity models are presented in a subsequent paper, Part 2.

2 Methodology

The conceptual model of the bottom boundary layer under a progressive wave is sketched in Figure 1. Here we consider a small control volume at the sea bed under a much larger wavelength surface wave, e.g., length $\lambda \sim 100$ m, and height $H = 2\eta \sim 2$ m, propagating at a velocity C_{ph} in a water depth $h \sim 5$ m. The wall at the bottom boundary is considered to be smooth.

A three-dimensional time-dependent numerical model [*Slinn and Riley*, 1998] has been applied to conduct numerical simulations of the turbulent wave bottom boundary layer. The model is based upon the incompressible Navier-Stokes equations with an external barotropic pressure gradient, $F_x = -\frac{1}{\rho}\frac{\partial p_\infty}{\partial x} = \frac{\partial U_\infty}{\partial t}$, added to the x-momentum equation to force current external to the boundary layer, where p_∞ and U_∞ are the pressure and fluid velocity above the boundary layer, respectively.

The conservation equations for mass and momentum in the boundary layer are, respectively,

$$\frac{\partial u}{\partial x} + \frac{\partial v}{\partial y} + \frac{\partial w}{\partial z} = 0, \tag{1}$$

$$\frac{\partial u}{\partial t} + u\frac{\partial u}{\partial x} + v\frac{\partial u}{\partial y} + w\frac{\partial u}{\partial z} = -\frac{1}{\rho}\frac{\partial p_t}{\partial x} + \nu(\frac{\partial^2 u}{\partial x^2} + \frac{\partial^2 u}{\partial y^2} + \frac{\partial^2 u}{\partial z^2}) + F_x, \tag{2}$$

$$\frac{\partial v}{\partial t} + u\frac{\partial v}{\partial x} + v\frac{\partial v}{\partial y} + w\frac{\partial v}{\partial z} = -\frac{1}{\rho}\frac{\partial p_t}{\partial y} + \nu(\frac{\partial^2 v}{\partial x^2} + \frac{\partial^2 v}{\partial y^2} + \frac{\partial^2 v}{\partial z^2}), \tag{3}$$

$$\frac{\partial w}{\partial t} + u\frac{\partial w}{\partial x} + v\frac{\partial w}{\partial y} + w\frac{\partial w}{\partial z} = -\frac{1}{\rho}\frac{\partial p_t}{\partial z} - g + \nu(\frac{\partial^2 w}{\partial x^2} + \frac{\partial^2 w}{\partial y^2} + \frac{\partial^2 w}{\partial z^2}), \tag{4}$$

where the components of the fluid velocity (u, v, w), respectively along the x-, y-, and z-axis, and the total pressure p_t are the unknowns. The Cartesian coordinates (x, y, z) are respectively aligned across-shore, along-shore, and vertically, positive upwards, g is the gravitational acceleration, ρ the constant fluid density, ν the kinematic viscosity, and F_x the x-component of a body force. The total pressure field can be written as $p_t = p_0 + p$, where p_0 is a reference state in hydrostatic balance with the background density field,

e.g.,

$$p_0 = -\rho g z. \tag{5}$$

The governing equations may be nondimensionalized as follows

$$x^* = \frac{x}{L}, \qquad u^* = \frac{u}{U}, \qquad t^* = t\frac{U}{L}, \qquad p^* = \frac{p}{\rho U^2}, \qquad F_x^* = F_x\frac{L}{U^2}, \tag{6}$$

where U is the characteristic velocity, L a characteristic length scale, and the pressure p is nondimensionalized with the dynamic pressure. Dropping the *'s, using the material derivative, $\frac{D}{Dt} = \frac{\partial}{\partial t} + u\frac{\partial}{\partial x} + v\frac{\partial}{\partial y} + w\frac{\partial}{\partial z}$, and subtracting (5) from the z-momentum equation (4), the governing equations can be rewritten in nondimensional form

$$\frac{\partial u}{\partial x} + \frac{\partial v}{\partial y} + \frac{\partial w}{\partial z} = 0, \tag{7}$$

$$\frac{Du}{Dt} = -\frac{\partial p}{\partial x} + \frac{1}{Re}(\frac{\partial^2 u}{\partial x^2} + \frac{\partial^2 u}{\partial y^2} + \frac{\partial^2 u}{\partial z^2}) + F_x, \tag{8}$$

$$\frac{Dv}{Dt} = -\frac{\partial p}{\partial y} + \frac{1}{Re}(\frac{\partial^2 v}{\partial x^2} + \frac{\partial^2 v}{\partial y^2} + \frac{\partial^2 v}{\partial z^2}), \tag{9}$$

$$\frac{Dw}{Dt} = -\frac{\partial p}{\partial z} + \frac{1}{Re}(\frac{\partial^2 w}{\partial x^2} + \frac{\partial^2 w}{\partial y^2} + \frac{\partial^2 w}{\partial z^2}), \tag{10}$$

where the Reynolds number is given by

$$Re = \frac{UL}{\nu}. \tag{11}$$

The model dimensions of the domain are $L^{(x)}$, $L^{(y)}$, and $L^{(z)}$ along the x-, y-, and z-axis, respectively. Experiments have been conducted using, for example, $L^{(x)} = 10$ cm, $L^{(y)} = 7.5$ cm, and $L^{(z)} = 5$ cm. In order to simplify lateral boundary conditions, the model geometry is made periodic in the x- and y-directions such that

$$(u, v, w, p)(x, y, z, t) = (u, v, w, p)(x + L^{(x)}, y, z, t), \tag{12}$$

$$(u, v, w, p)(x, y, z, t) = (u, v, w, p)(x, y + L^{(y)}, z, t). \tag{13}$$

The periodicity allows only certain discrete spatial modes to exist in the computed flow. If the dominant modes present, however, are small compared to the periodic

dimensions, this approximation can be accepted. The dimension of the domain in the x-direction, $L^{(x)}$, is small compared to the wavelength, λ, and justifies the approximation that the time dependent forcing through the pressure gradient acts uniformly on the control volume. A consequence of the periodic approximation in the x-direction is that boundary layer streaming [*Batchelor*, 1967] is not allowed in the model. No slip (and no penetration) boundary conditions are specified at the bottom boundary ($z = 0$) with

$$(u, v, w)(x, y, 0, t) = 0. \tag{14}$$

The boundary conditions on pressure at the bottom and top boundaries are determined using the projection method detailed in *Slinn and Riley* [1998]. An open boundary condition at the upper boundary is implemented using a Rayleigh damping sponge layer [*Durran et al.*, 1993] utilizing 10 percent of the total grid points in the vertical direction and absorbs any disturbances propagating upwards from the boundary layer, such that

$$u(x, y, L^{(z)}, t) = U_\infty(t), \tag{15}$$

$$v(x, y, L^{(z)}, t) = V_\infty(t), \tag{16}$$

$$w(x, y, L^{(z)}, t) = 0, \tag{17}$$

$$p(x, y, L^{(z)}, t) = 0. \tag{18}$$

In this model, the simple harmonic oscillatory wave induced velocity above the seabed is given by $U_\infty(t) = U_m \sin(\omega t + \varphi)$. This velocity is commonly examined in the range 10-100 cm s^{-1}. Because of the oscillatory behavior of the external flow, an inflectional instability is induced during phases of flow deceleration and flow reversal. For flows in which the boundary layer becomes turbulent, the typical turbulent boundary layer thickness, δ_τ, is of the order of 0.5-5 cm. These values lead to typical boundary layer thickness Reynolds numbers, $Re_{\delta_\tau} = \dfrac{U_m \delta_\tau}{\nu}$, between 500 and 50,000. The various Reynolds numbers based on amplitude, frequency, and boundary layer thicknesses are presented for the several numerical experiments in Table 1.

The basic numerical model is described in detail in *Slinn and Riley* [1998]. The model uses uniform grid spacing in the x- and y-directions and non-uniform or clustered grid spacing along the z-axis, for better resolution in the strong shear layer at the bottom boundary. A variety of numerical schemes are used in the model. The spatial derivatives are calculated using Hermitian compact or Padé series techniques, with sixth-order accuracy [*Lele*, 1992].

Low level white noise is included as part of the initial conditions, and the flow is generally started from rest at $t = 0$ s. The numerical scheme employs the pressure projection method, implemented with a variable time step third-order Adams-Bashforth scheme to achieve high temporal accuracy. The pressure field is determined by solving the Poisson equation using Fourier transforms in the lateral x- and y-directions and a fourth-order direct solution method in the vertical z-direction.

For the higher Reynolds number experiments, e.g., for $Re_{\delta_\tau} > 10{,}000$, the model incorporates additional artificial numerical dissipation at the smallest resolved length scales. This is performed by adding hyperviscosity terms to the momentum equations, e.g., $\mu\nabla^6 \overrightarrow{u}$, with $\mu \ll 1$, to filter energy at poorly resolved scales. Since the boundary layer dynamics are not microscale driven, modeling subgrid-scale numerical dissipation by a dissipation with length scales less than about 1 mm, the addition of hyperviscosity does not dominate or invalidate the results obtained.

We define here a number of averaging operators and variables to be employed later in the discussion of results. The time average, the horizontal average in the x- and y-directions, and the volume average of a quantity $G(x, y, z, t)$ are respectively given by

$$\overline{G} = \frac{1}{\triangle t} \int_{t_i}^{t_f} G(x, y, z, t) dt, \tag{19}$$

$$\langle G \rangle = \frac{1}{L^{(x)} L^{(y)}} \int_0^{L^{(y)}} \int_0^{L^{(x)}} G(x, y, z, t) dx \; dy, \tag{20}$$

$$\langle\langle G\rangle\rangle = \frac{1}{L^{(z)}} \int_0^{L^{(z)}} \langle G\rangle dz, \tag{21}$$

where $\triangle t = t_f - t_i$. Variables such as the velocity may be divided into mean horizontally-averaged and fluctuating parts as defined by

$$G(x, y, z, t) = \langle G\rangle + G'(x, y, z, t). \tag{22}$$

The kinetic energy dissipation rate is given in a three-dimensional flow by

$$\begin{aligned} \varepsilon(x, y, z, t) = \quad \nu \quad & \Big\{ 2\frac{\partial u}{\partial x}^2 + 2\frac{\partial v}{\partial y}^2 + 2\frac{\partial w}{\partial z}^2 + \Big(\frac{\partial v}{\partial x} + \frac{\partial u}{\partial y}\Big)^2 + \\ & \Big(\frac{\partial w}{\partial y} + \frac{\partial v}{\partial z}\Big)^2 + \Big(\frac{\partial u}{\partial z} + \frac{\partial w}{\partial x}\Big)^2 \Big\}. \end{aligned} \tag{23}$$

3 Results

Results and findings of numerical experiments conducted to examine turbulent wave bottom boundary layers are presented below.

3.1 Model Calibration

We pursue high-resolution three-dimensional numerical experiments of the wave bottom boundary layer to complement previous studies. Most of the numerical experiments are well resolved (cf. Section 3.3) and can be considered direct numerical simulations [*Moin and Mahesh*, 1998] where no sub-grid scale turbulence model is necessary. In these cases the results of the numerical experiments can be considered nearly as valid as laboratory experiments. The highest Reynolds number experiments attempted are near the limits of Direct Numerical Simulations (DNS) for this grid resolution and the model results are interpreted with some caution but still considered qualitatively and semi-quantitatively accurate. It was determined that the physical location of the least well resolved flow properties in these cases was a few centimeters above the bottom boundary. In these few cases the trends indicated by comparison with the lower Reynolds number simulations are still justified. In addition, the first order quantities such as mean velocity profiles and wall shear stress are still considered accurate but the precise magnitude of second order quantities such as turbulent kinetic energy and energy dissipation rates may have somewhat larger error bars. An advantage in retaining accuracy in the estimates of net kinetic energy dissipation rates is that the flux of energy to small dissipative scales cascades down from well resolved spatial scales.

We do not present here detailed comparison of the numerical experiments with related laboratory results. Most of the published laboratory experiments deal with higher frequency waves or rough boundaries or both. Because of difficulties in the past of making accurate non-intrusive measurements in the near wall region it was also rare to

find laboratory measurements of the boundary layer structure in regions closer than 1 mm to the wall, where the DNS model indicates much of the shear and boundary layer structures originate. Also because of the model's periodic boundary conditions in the lateral directions, the model is not identical to related laboratory experiments that contain weak horizontal gradients in the mean pressure field under the waves. Our model runs are perhaps most similar to the one-dimensional boundary layer models, to which extensive comparison is made in the subsequent paper (Part 2) except that we employ a more sophisticated and computationally expensive turbulence closure model, i.e., direct simulation of the small scale turbulence. We first validated our model against exact solutions derived by *Stokes* [1845] and *Panton* [1968] for laminar flow. Close agreement was also obtained by comparison with classical results for turbulent boundary layer profiles for steady uni-directional flow over a flat plate [*Schlichting*, 1968] to validate turbulent aspects of the model. We also present extensive comparison in the second paper (Part 2) of our mean boundary layer profiles to the models of *Grant and Madsen* [1979, 1986] and *Trowbridge and Madsen* [1984] that were developed and calibrated mostly in comparison with oscillatory flow over rough boundaries.

3.2 Free Stream Velocities

3.2.1 Experiments

The three-dimensional model has been used with different free-stream velocity time-series described in Table 1. Four sets of experiments have been conducted to examine boundary layer response to different wave forcing conditions. The first two sets of experiments have utilized simple harmonic waves, Figure 2 (a). Set one (Cases 1-4) held the wave period fixed at $T = 5$ s and varied the wave amplitude. The second set of experiments (Cases 2, 5-8) held the wave amplitude fixed and varied the wave period, from $T = 3$ s to $T = 12.5$ s. This set also includes the case of a steady flow, i.e., an infinite-period wave

(Case 8), Figure 2 (e). The third set of experiments (Cases 9-11) analyzes the transition at flow reversal, for different types of waves. These are represented in Figure 2, e.g., (b) a skewed wave (Case 9); (c) a complex frequency wave (Case 10); and (d) a wave packet, the product of two sine functions of different frequencies (Case 11). The fourth set of experiments (Cases 12-14) examines the interaction of a mean current, V_∞, in the direction perpendicular to the direction of wave oscillation.

3.2.2 Physical Relevance

The near-bed free-stream velocity fluctuations used in the numerical experiments are in the range of conditions commonly produced in littoral waters in nature. In Table 2, we list combinations of surface wave conditions at two arbitrarily chosen water depths that would produce boundary layer currents similar to those used in the numerical experiments.

The horizontal velocity in the x-direction under a linear surface gravity wave is

$$u(z) = \frac{gHk}{2\omega} \frac{\cosh k(h+z)}{\cosh(kh)} \cos(kx - \omega t), \tag{24}$$

where H is the wave height ($H = 2\eta$), h the water depth, k the wavenumber, and ω is defined by the dispersion relation [*Dean and Dalrymple*, 1991]

$$\omega^2 = gk \tanh(kh). \tag{25}$$

For a specified set of conditions h, T, and H, we determine $u_{z=-h}$, the wave induced horizontal velocity just above the bottom boundary layer,

$$u_{z=-h} = \frac{gHk}{2\omega} \frac{1}{\cosh(kh)}. \tag{26}$$

The maximum velocity induced under the waves, is also listed in Table 2 determined by

$$u_{z=0} = \frac{gHk}{2\omega}. \tag{27}$$

We take $z = 0$ at the mean free surface for this illustration (though $z = 0$ at the sea bed in the simulations).

All of the experimental conditions studied with the three-dimensional model can occur under moderate conditions in the ocean. The wavelength, λ, maximum wave velocity, $u_{z=0}$, and the boundary layer velocity, $u_{z=-h}$, are plotted in Figure 3 as functions of the distance from the shore x, for $200 < x < 800$ m, for a water depth $h(x)$ with a 1% slope, for different values of the wave period T. The wave height $H = 2$ m is taken here to be approximately constant. The wavelength, λ, Figure 3 (b), increases slowly as the water depth $h(x)$ increases, as shown in Figure 3 (a), and is larger when the wave period T increases. The maximum velocity under the waves, $u_{z=0}$, calculated from (27), decreases with x as λ increases. The near-bed wave induced current velocity, $u_{z=-h}$, is larger as the period increases, however, for $x < 200$ m, in shallow water for all these wave periods, the velocity does not vary significantly as T increases.

3.3 Basic Flow Features

Although the water motion induced by natural waves is not simple harmonic, it is a useful starting point to study a monochromatic wave induced flow (Case 1). The modeled domain uses the following dimensions $L^{(x)} = 0.1$ m, $L^{(y)} = 0.075$ m, and $L^{(z)} = 0.05$ m and a grid resolution of 256 x 128 x 130 grid points in the x-, y- and z-directions, respectively. The flow is initialized with low-energy white noise and forced with a pressure gradient that produces a free-stream velocity with a 5-second period and a maximum amplitude of 0.80 m s^{-1}, i.e., $U_\infty(t) = 0.80 \sin(\frac{2\pi}{5}t)$ m s^{-1}. The free stream velocity is plotted in Figure 2 (a).

3.3.1 Velocity Vectors

Side and top views of the velocity field during phases of flow deceleration and flow reversal are illustrated in Figure 4. For clarity, the figures do not show velocity vectors at all

the grid points in each direction. The near-wall flow is represented in Figure 4 (a). The flow is well-organized and approximately two-dimensional; the velocity is not strongly variable in the x-direction. The second grid point is less than 0.1 mm from the boundary and the strong shear layer at the bottom is resolved with approximately 15 grid points. Along-stream streaks of lower speed flow are seen in the top view of the velocity field located at $z_0 = 0.27$ cm in panel (b). These streaks are often observed in laboratory experiments of boundary layers [*Sarpkaya*, 1993] and are evident during transition before turbulence develops. We note that $\dfrac{\partial u}{\partial y} \neq 0$.

The velocity field structure shown in Figures 4 (c) and (d), during a turbulent event near flow reversal, is complex and disorganized. Note that the reference vector length representing velocities of 0.11 m s^{-1} is longer in the bottom panels than in the top panels. In Figure 4 (c), the velocity magnitude for $z > 4$ cm is almost zero and for $z < 1$ cm, about 0.1 m s^{-1}.

The boundary layer thickness can be visually estimated to approximately $\delta'_\tau = 4$ cm. We take this opportunity to discuss the complexity of defining the boundary layer thickness. The boundary layer is generally defined as the distance from the wall where the velocity differs by one percent from the free stream velocity. In oscillatory flow, it is, however, difficult to determine this value because of the overshoot of the velocity near the bed. In the present work, the boundary layer thickness is visually estimated from horizontally averaged turbulent kinetic energy contours by considering a mean value, e.g, in Figure 6 (a), $\delta_\tau = 2$ cm and not 3 or 4 cm.

The flow near the wall, illustrated in Figure 4 (d), is strongly three-dimensional. A rough estimate of the horizontal length scales of typical flow features is 1 cm.

3.3.2 Kinetic Energy Dissipation Rates

Kinetic energy dissipation rate contours, given by equation (23), are plotted for different phases of the wave period in Figure 5. The left panels show results on a vertical x-z plane located at $y_0 = 3.75$ cm and the right panels depict a horizontal x-y plane parallel to the wall at $z_0 = 0.30$ cm. The scale of these figures has been chosen in order to emphasize the structure of the eddies and not the intensity of the kinetic energy dissipation rate. The turbulence is episodic in nature, going through mixing phases approximately twice per wave period with strongest turbulent production near flow reversal. In this experiment, every 2.5 seconds the flow changes direction and 1.25 seconds after flow reversal the mean flow achieves its maximum amplitude.

At $t = 12.44$ s, which corresponds closely to a phase of flow reversal, the turbulence achieves its maximum intensity, as shown in Figures 5 (a) and (b), and then decays as the flow accelerates in the opposite direction. At $t = 13.82$ s, the flow velocity is near maximum and the turbulence is minimum, as plotted in Figures 5 (c) and (d). Figure 5 (c) doesn't show significant levels of turbulence and Figure 5 (d) illustrates some characteristic streaks in the alongstream direction observed in contours of the dissipation rate. Note that even though turbulence levels are decreased at this phase, the dissipation rates, near the bottom boundary and integrated over the domain, are now much stronger than at $t = 12.44$ s. Finally, at $t = 14.60$ s, before flow reversal, the flow is decelerating, destabilizing the boundary layer and developing patches of turbulence near the wall [*Gad-El-Hak et al.*, 1984], as shown in Figures 5 (e) and (f). Streaks in the x-direction can still be observed in Figure 5 (f), with bursts of turbulence that originate near $y_0 = 4$ cm, spreading laterally and engulfing the surrounding fluid.

In this experiment, the x-z planes show variations in the boundary layer thickness, δ_τ, from approximately 0.5 cm during periods of laminar flow to 2 cm at flow reversal, as shown in Figures 5 (c) and (e), respectively.

It can be noted that dissipation rate contours are approximately equal to the vorticity magnitude squared $|\boldsymbol{\omega}|^2$ [*Tennekes and Lumley*, 1972], where $\boldsymbol{\omega} = \nabla \mathrm{x} \mathbf{u}$ is the vorticity vector and $\mathbf{u}$ the fluid velocity vector. Regions of high dissipation rate represent cores of small eddies or vortices. A visual qualitative estimate of the eddy diameters as a function of time can be made. The top views, panels (b), (d) and (f), indicate typical eddy diameters and cross-stream coherent structure length scales in the range of 0.1-2.0 cm, depending of the wave phase.

3.3.3 Turbulent Kinetic Energy

The horizontally averaged turbulent kinetic energy, as a function of height, z, and time, t, is shown in Figure 6 (a), where

$$\langle TKE(z,t) \rangle = \frac{1}{2} \left\langle u'^2 + v'^2 + w'^2 \right\rangle , \tag{28}$$

where u', v', and w' are the velocity fluctuations about the horizontally averaged flows $\langle u \rangle (z)$. The turbulence is weaker during the first two wave periods of the experiment, as initial transients develop before achieving a quasi-steady behavior for $t > 10$ s. Initial transients in mean velocity profiles, growth rates of linear instabilities, and initial levels of background noise are important at early times. In general, as illustrated in Figure 6 (a), a quasi-steady flow response to periodic wave forcing is achieved after two or three flow reversals. Then, turbulent bursts become episodic in nature, approximately twice per wave period (i.e., every 2.5 s). Turbulence initiates near the wall during phases of flow deceleration, achieves its maximum intensity and vertical excursion just after flow reversal and decays rapidly as the flow accelerates in the opposite direction [*Piomelli et al.*, 2000]. The decay of turbulence is seen to be more sudden than the onset of turbulence. Turbulence is strong for approximately half a wave cycle depending on the z-location. The turbulence originates very close to the boundary wall, at heights of approximately 0.1 cm, and significant turbulent kinetic energy extends to heights of

approximately 2 cm, thus the turbulent boundary layer thickness can be estimated at $\delta_\tau = 2$ cm. Contour levels were selected to emphasize the time dependent structure of turbulent regions rather than the turbulence intensity.

The maximum horizontally averaged turbulent kinetic energy $\langle TKE_m(t) \rangle$ and the volume averaged mean turbulent kinetic energy $\langle \langle TKE(t) \rangle \rangle$ as a function of time are shown in Figure 6 (b). The quantity $\langle \langle TKE(t) \rangle \rangle$ has been calculated over the domain $0 < z < 2$ cm, the estimate for the boundary layer thickness, δ_τ, the turbulent kinetic energy being small above this height. As shown in the figure, the mean turbulence achieves its maximum intensity just after flow reversal, with a maximal value of 0.0088 $\mathrm{m^2\ s^{-2}}$ which occurs at a height of $z = 0.1$ cm.

For scaling purposes only, estimates of velocity perturbations can be made assuming that the flow is isotropic, i.e., $u' \sim v' \sim w'$. In this case, the turbulent kinetic energy is approximately $\langle \langle TKE(t) \rangle \rangle \sim \frac{3}{2} u'^2$, which suggests that for a volume averaged turbulent kinetic energy $\langle \langle TKE(t) \rangle \rangle = 0.003$ $\mathrm{m^2\ s^{-2}}$, the velocity fluctuations are of the order $u' = 0.04$ $\mathrm{m\ s^{-1}}$. For the maximum local value of horizontally averaged turbulent kinetic energy $\langle TKE_m(t) \rangle = 0.0088$ $\mathrm{m^2\ s^{-2}}$, the average velocity fluctuations would be approximately $u' = 0.07$ $\mathrm{m\ s^{-1}}$. In this experiment, the maximum free-stream velocity is $U_m = 0.8$ $\mathrm{m\ s^{-1}}$ but peak levels of turbulence occur near phases before and after flow reversal when typical free-stream velocities, $U_\infty < 0.3$ $\mathrm{m\ s^{-1}}$, and relatively near the boundary where $\langle u \rangle(z) < U_\infty$.

3.3.4 Kinetic Energy and Dissipation Rate Spectra

Volume averaged kinetic energy and dissipation rate spectra in the x- and y-directions at $t = 12.00$ s, i.e., at the time of maximum turbulence during the simulation (e.g., Figure 6 (b)) are shown in Figure 7. This experiment was conducted with a grid resolution of 256 x 128 x 130 grid points which translate to 128 k_x wavenumbers in x and 64 k_y

wavenumbers in y and horizontal grid spacing of approximately 0.4 mm. The volume average total kinetic energy is given by

$$KE = \frac{1}{2}\langle\langle u^2 + v^2 + w^2\rangle\rangle, \tag{29}$$

and the x-, y-, and z-component volume average kinetic energies are labeled u^2 for $\frac{1}{2}\langle\langle u^2\rangle\rangle$, v^2 for $\frac{1}{2}\langle\langle v^2\rangle\rangle$, and w^2 for $\frac{1}{2}\langle\langle w^2\rangle\rangle$, respectively. The kinetic energy spectra and its three components u^2, v^2, and w^2, and straight lines representing $k^{-5/3}$ and k^{-3} are represented in Figure 7 (a) and (b) in the x- and y-directions, respectively. The method of determining these quantities are detailed in Appendix A.

For $\frac{k_x}{2\pi} > 5$ dm^{-1}, the flow is approximately horizontally isotropic, i.e., $u^2 \sim v^2 \sim w^2$ as seen in Figures 7 (a) and (b), but for $\frac{k_x}{2\pi} < 5$ dm^{-1}, greater energy content is contained in u^2 than in v^2 or w^2. Energy levels in wavenumbers in the range $3 < \frac{k_x}{2\pi} < 20$ dm^{-1} approximately follow the $k^{-5/3}$ slope curve, commonly associated with the inertial subrange of turbulence cascade. For higher wavenumbers, $\frac{k_x}{2\pi} > 20$ dm^{-1}, the energy content decreases rapidly. For $15 < \frac{k_x}{2\pi} < 40$ dm^{-1}, the kinetic energy curves approximately follow the k^{-3} slope, which is typical of the small scale dissipation range. The mean flow, which is represented by a wavenumber $0 + \epsilon$, ϵ being small, has significantly greater energy. Approximately, 7 orders of magnitude difference in energy content can be noticed between well-resolved scales, i.e., for $\frac{k_x}{2\pi} < 7$ dm^{-1}, and smallest resolved scales on computational mesh, e.g., $\frac{k_x}{2\pi} \sim \frac{2}{3}(128) = 86$ dm^{-1}. This difference indicates that the model is satisfactorily resolved during the turbulent bursts.

Similar results are obtained from the kinetic energy spectra decomposed in the y-direction shown in Figure 7 (b). At this time, the flow is not isotropic in the y-direction as u^2 is greater than v^2 or w^2. Energy content in wavenumbers in the range $3 < \frac{k_y}{2\pi} < 12$ dm^{-1} approximately follows the $k^{-5/3}$ slope curve, and for higher wavenumbers, $\frac{k_y}{2\pi} > 30$ dm^{-1}, the energy content decreases rapidly. For $15 < \frac{k_y}{2\pi} < 25$ dm^{-1}, the kinetic energy

curves approximate the k^{-3} slope.

Dissipation rates as a function of wavenumber can be estimated from $k_x^2 KE$ or $k_y^2 KE$ as shown, respectively, in log-log form in panels (c) and (d) or in a linear form in panels (e) and (f). Figure 7 (c) shows a peak in the dissipation rates decomposed in the x-direction near $\frac{k_x}{2\pi} = 10$ dm^{-1} and a rapid decline for higher wavenumbers. The majority of dissipation occurs in the wave band $5 < \frac{k_x}{2\pi} < 20$ dm^{-1}. Wavenumbers in the range $\frac{k_x}{2\pi} > 30$ dm^{-1} are in the far dissipation range. Figure 7 (e) illustrates more quantitatively the dissipation rate maxima in the range $5 < \frac{k_x}{2\pi} < 15$ dm^{-1}. For $\frac{k_x}{2\pi} > 30$ dm^{-1}, the subgrid-scale filter [*Slinn and Riley*, 1998] has increased influence. The decomposition of the dissipation rate spectra in the y-direction in the log-log plot in Figure 7 (d) shows a peak in the dissipation rate and Figure 7 (f) gives more precisely the range of this maxima for $5 < \frac{k_x}{2\pi} < 12$ dm^{-1}.

3.3.5 Resolved and Subgrid Dissipation Rates

The volume averaged kinetic energy dissipation rates measured from the three-dimensional model at well resolved scales and from the subgrid scale filter are displayed in Figure 8. These are plotted to show the absolute value of the dissipation rates as a function of time; these quantities, however, should be negative, meaning a loss of kinetic energy from the flow. The dissipation rate is a strong function of time and maximum during phases of strong flow. Integrated over time, 93.6% of the kinetic energy dissipation occurs at well-resolved scales and 6.4% is through the subgrid scale filter. Comparison of these magnitudes shows that most of the dissipation has been satisfactorily resolved for this experiment. This experiment is one of the highest Reynolds number attempted in this study (Table 1) and thus represents a "worst case" in which the subgrid scale filter makes a relatively large contribution to net dissipation. Thus it can be concluded that the flows are sufficiently resolved for the flow features of interest here for the experiments

presented below. The maximum energy removal by filtering occurs at approximately $t = 12.0$ s and $t = 14.5$ s, when, comparing to Figure 6 (b), the volume averaged turbulent kinetic energy is maximum and the turbulence has generally cascaded down to smaller marginally resolved scales less than 1 mm. Additional discussion of numerical resolution issues and the Kolmogorov length scale is included in Appendix B.

The Kolmogorov length scale varies depending on the energy in the mean flow. In the numerical experiments of this work, it is generally somewhat smaller than the smallest eddies that can be well represented on the grid and a small net portion ($\sim$ 2-5 %) of subgrid scale energy dissipation is produced by the filter.

3.3.6 Wall Shear

The wall shear component $\frac{\partial u}{\partial z}\Big|_w$ in the x-y plane is plotted for two phases of the flow, near maximum flow in Figure 9 (a) and near flow reversal in Figure 9 (b). These figures indicate the spatial variability of the wall shear stress given by $\overrightarrow{\tau}_w = \mu \frac{\partial u}{\partial z}\Big|_w \widehat{i} + \mu \frac{\partial v}{\partial z}\Big|_w \widehat{j}$. This parameter is important to ocean problems because sediment suspension and movement are dependent on τ_w. Figure 9 (a) illustrates two-dimensional along-stream streaks, as observed in the velocity field in Figure 4 and dissipation rate in Figure 5. The wall shear component $\frac{\partial u}{\partial z}\Big|_w$ in Figure 9 (a), varies by approximately a factor of 2 and is not homogeneous in y during periods of maximum flow. Spatial variation is even larger near flow reversal as shown in Figure 9 (b). Here, randomly distributed three-dimensional coherent structures, features of a turbulent event, are observed with characteristic length scales of approximately 0.5-1 cm, similar to the eddy sizes observed in Figure 5. Panel (b) occurs during a phase of transitioning flow as the turbulence spreads across the boundary layer in y and has not yet engulfed the fluid in the region $2 < y < 4$ cm.

In a laminar flow with a free stream velocity of the form $U_\infty(t) = U_m \sin(\omega t)$, the bed shear stress is given by $\frac{\tau_w}{\rho} = \nu \frac{\partial u}{\partial z}\Big|_{z=0} = \frac{\nu U_m}{\delta_s} \sin(\omega t + \pi/4)$ [*Fredsoe and Deigaard*,

1992]. From this equation, it can be noticed that there is a phase lag of 45° between the shear stress τ_w and the free-stream velocity $U_\infty(t)$ [*Jonsson*, 1980]. This phase difference is introduced because a barotropic adverse pressure gradient (constant with depth) can more easily decelerate that part of the flow which is located close to the bed in the boundary layer, since the flow has lower inertia in this region. In the turbulent case, the near-wall velocities are generally slower than in the laminar case, especially during phases close to flow reversal, and the boundary layer is thicker, because of the vertical exchange of momentum by the eddies. For this reason, the phase shift between the bed shear stress τ_w and the free stream velocity $U_\infty(t)$ should not be as large in the turbulent case.

A plot of the root mean squared value of the wall shear stress and the absolute value of free stream velocity is given in Figure 10 in order to quantify the turbulent phase shift. By calculating maximum time-lagged cross correlations

$$R_{\tau_w U_\infty} = \frac{\langle\langle \tau_w(t) \rangle\rangle \, \langle\langle U_\infty(t-\phi) \rangle\rangle}{\sigma_{\tau_w} \sigma_{U_\infty}}, \tag{30}$$

the wall shear stress τ_w has been found to be ahead of the free stream velocity $U_\infty(t)$ by approximately 30° for this experiment. This phase shift is comparable to values previously reported in the literature [*Jonsson*, 1980] from laboratory measurements.

3.4 Reynolds Number Dependence

The model has been forced by simple harmonic free stream velocities of different wave amplitudes, U_m, resulting in different Reynolds numbers based on the wave amplitude, $Re = \dfrac{U_m L^{(z)}}{\nu}$. The characteristics of these experiments are given in Table 1, as Cases 1-4.

3.4.1 Turbulent Kinetic Energy for Different Reynolds Numbers

The horizontally averaged turbulent kinetic energy for different amplitudes of forcing velocity, $U_m = 0.60$ m s^{-1} (Case 2), 0.40 m s^{-1} (Case 3), and 0.20 m s^{-1} (Case 4) are shown in Figure 11 (a), (b), and (c), respectively, and can be compared with the 0.80 m s^{-1} sine wave (Case 1), shown in Figure 6 (a).

The comparison of the intensity of these quantities shows that as the wave amplitude, U_m, decreases (i.e., wave amplitude Reynolds number decreases), the turbulent kinetic energy decreases. The strength of the turbulent kinetic energy and the turbulent boundary layer thickness, estimated to $\delta_\tau = 1$ cm, in Figure 11 (a) are qualitatively similar to Figure 6 (a). Figures 11 (b) and (c), have lower scales for the contour legend by approximately three orders of magnitude compared to Figures 6 (a) and 11 (a), and do not develop bursts of turbulence. The weak fluctuations seen in panels (b) and (c) for $t < 5$ s are likely due to temporary amplification of the small perturbations (white noise) introduced in the beginning of each run and which can grow and organize when linear instabilities are present in the velocity profiles. These fluctuations eventually decay and vanish after a few wave periods. Comparing the values of the frequency Reynolds numbers of these different cases, given in Table 1, to the transitional frequency Reynolds number given in the literature, $Re_{\omega trans} = 100{,}000$ [*Jonsson*, 1980], it can be concluded that Case 1 and Case 2, in which $Re_\omega = \dfrac{A_m^2 \omega}{\nu} = 510{,}000$ and $Re_\omega = 290{,}000$, respectively, should be turbulent as their frequency Reynolds numbers are larger than $Re_{\omega trans}$. Case 3 can be considered in the transitional range as its Reynolds number $Re_\omega = 130{,}000$ is close to $Re_{\omega trans}$ and Case 4 is expected to be, and remains laminar with $Re_\omega = 32{,}000$. We note that our mathematically smooth wall surface should probably have a lower transitional Reynolds number than the laboratory experiments which likely have small roughness or experience ambient vibrations. The laminar to turbulent

transition occurs, in the model, for $Re = \dfrac{U_m L^{(z)}}{\nu} \approx 25{,}000$.

Cases 1-4 have $T = 5$ s, with different U_m. The magnitude of the deceleration of the wave forcing, $a = \dfrac{\partial U_\infty(t)}{\partial t}$, obviously increases as the wave amplitude increases in these cases. It has been shown [e.g., *Gad-El-Hak et al.*, 1984; *Piomelli et al.*, 2000] that the magnitudes of the acceleration and deceleration phases are important parameters in the response of turbulence in a boundary layer. When the deceleration is weak or acceleration is strong, turbulence production is inhibited. These results suggest that for this wave frequency, decelerations less than 0.5 m s^{-2} are insufficient to overcome viscous damping of inflectional shear instabilities present near the wall during phases of deceleration and flow reversal.

3.4.2 Volume Mean Square Shear for Different Reynolds Numbers

The components of the volume mean square shear for the x-component of velocity, u, for Cases 1-4 are displayed as a function of time in Figures 12 (a), (b), and (c). Comparing the intensity of the mean square shears, it can be noticed that typically

$$\left\langle\left\langle \frac{\partial u}{\partial z}^2 \right\rangle\right\rangle \sim 40 \left\langle\left\langle \frac{\partial u}{\partial y}^2 \right\rangle\right\rangle \sim 400 \left\langle\left\langle \frac{\partial u}{\partial x}^2 \right\rangle\right\rangle . \tag{31}$$

Note that $\left\langle\left\langle \dfrac{\partial u}{\partial y}^2 \right\rangle\right\rangle$ is larger than $\left\langle\left\langle \dfrac{\partial u}{\partial x}^2 \right\rangle\right\rangle$ during periods of laminar flow, that is when streamwise streaks are evident, $\dfrac{\partial u}{\partial y} \neq 0$, as seen in Figure 4 (b). Based on equation (31), it is evident why most of the energy dissipation comes from the term $\left\langle\left\langle \dfrac{\partial u}{\partial z}^2 \right\rangle\right\rangle$. Exponential growth in $\left\langle\left\langle \dfrac{\partial u}{\partial x}^2 \right\rangle\right\rangle$ and $\left\langle\left\langle \dfrac{\partial u}{\partial y}^2 \right\rangle\right\rangle$, for 3.5 s $< t <$ 5 s, shows evidence of linear instabilities present in the boundary layer flow during flow deceleration, the flow being maximum at $t \sim 3.75$ s and decelerating thereafter. $\left\langle\left\langle \dfrac{\partial u}{\partial x}^2 \right\rangle\right\rangle$ decreases as a function of time for the lower Reynolds number experiments particularly for $Re = 20{,}000$ (Case 3) and $Re = 10{,}000$ (Case 4). For $Re = 20{,}000$, the three-dimensional aspects of

the flow decay in time from initial low level white noise. For Re = 20,000, $\left\langle \left\langle \frac{\partial u}{\partial x}^2 \right\rangle \right\rangle$ shows some small perturbations from t = 5 s, suggesting a flow near transition. The same comportment is observable in Figure 12 (b) with $\left\langle \left\langle \frac{\partial u}{\partial y}^2 \right\rangle \right\rangle$. Finally, $\left\langle \left\langle \frac{\partial u}{\partial z}^2 \right\rangle \right\rangle$, shown in Figure 11 (c) doesn't change significantly as a function of the Reynolds number and illustrates the periodic characteristic of the flow.

3.5 Wave Periods

Numerical experiments have been conducted for different wave periods, T, holding U_m = 0.8 m s^{-1} constant. The characteristics of these runs are presented in Table 1, comprising Cases 1, 5-8.

3.5.1 Turbulent Kinetic Energy for Different Wave Periods

The horizontally averaged turbulent kinetic energy for different wave periods, T = 3 s (Case 5), T = 8 s (Case 6), T = 12.5 s (Case 7), and $T = \infty$ (Case 8) are shown in Figures 13 (a), (b), (c), and (d), respectively, and can be compared with the five-second period wave (Case 1), shown in Figure 6 (a). Note that the scale in contour legend is not the same for panel (d). The comparison of the intensity of the turbulent kinetic energy shows that as the period T increases, or the frequency, $\omega = \frac{2\pi}{T}$, decreases, the flow becomes more turbulent and the turbulent boundary layer thickness increases, e.g., δ_τ = 0.5 cm for T = 3 s, δ_τ = 2.0 cm for T = 5 s, δ_τ = 2.5 cm for T = 8 s, δ_τ = 3.0 cm for T = 12.5 s, and δ_τ = 4 cm for $T = \infty$ (this is evident if the contour levels are decreased to be the same as the other panels, but causes the rest of the structure to be obscured). In Figure 13 (c), turbulence is almost continuous in the sense that each event persists for $z > 2$ cm until the next begins near $z < 0.5$ cm. In the first three panels, the turbulent kinetic energy levels are periodic. However, in Figure 13 (d), the flow stays turbulent for the steady flow, i.e., the flow can not be reorganized as in the oscillatory flows during

phases of flow acceleration. In the case of steady flow, the turbulence intensity becomes somewhat steady for $t > 12$ s.

Panel (d) represents the Rayleigh problem, an impulsively accelerated uniform flow over a flat plate. Initial attempts with the Rayleigh problem (not shown), using low-level white noise initialized with $[u'^2 + v'^2 + w'^2]^{1/2}_{rms} \sim 10^{-4} U_m$ remained laminar. Initial perturbations associated with boundary layer instabilities grew for a short period of time and then decayed. In this experiment, we used root mean squared velocity fluctuations of approximately $u'_{rms} \sim 0.03$ m s^{-1}.

In laboratory experiments of a spatially developing boundary layer over a flat plate, the Tolmein-Schlichting [*Schlichting*, 1968] instabilities have been found to develop when forced at unstable wavenumbers with a fluctuating ribbon over a smooth flat plate when $u' = 0.03 U_m$. When smaller amplitude perturbations are attempted, the flow response is similar to what is observed in our Rayleigh experiments with low level white noise fluctuations. Tolmein-Schlitching waves are not what lead to turbulence in our realization of the Rayleigh problem. The region of elevated velocity fluctuations shown in Figure 13 (d) for $4 < t < 7$ s are representative of streamwise streaks that grow and then decay before the flow transitions to turbulence at later time when hairpin vortices develop near $t = 9$ s that finally cause three-dimensionality to spread across the boundary layer.

Complicating the interpretation of the role of flow deceleration and acceleration, in understanding transitioning flows, it is noted that as the wave period, T, increases, the magnitude of the acceleration-deceleration, $a = \dfrac{\partial U_\infty(t)}{\partial t}$, decreases. In these experiments, it is the flow with weaker deceleration that become more turbulent. It has also been seen, however, that as T increases, the turbulence increases. Thus, it is suggested that the duration of deceleration phase can be more significant than its amplitude for different flow situations. In these cases, the frequency Reynolds number is still a useful predictor of flow transition, since Re_ω decreases as ω increases. For Case 5, $Re_\omega \approx$

300,000 with $T = 3$ s, and the flow is only weakly turbulent, compared to Cases 1, 6, and 7 with $T = 5$, 8, and 12.5 s with $Re_\omega \approx$ 510,000, 815,000, and 1,270,000 that are strongly turbulent.

3.6 Wave Shape

Numerical experiments have also been conducted for free-stream velocity time series that would be produced by different shapes of surface waves, a skewed (steep) wave, a complex frequency wave, and a wave packet, to study the flow response in the boundary layer to these variations. Characteristics of these flows are given in Table 1.

3.6.1 Turbulent Kinetic Energy for Different Wave Shapes

The horizontally averaged turbulent kinetic energy for different types of forcing, skewed wave, complex frequency wave, and wave packet (Cases 9-11) are shown in Figures 14 (a), (b), and (c), respectively.

The skewed wave forcing condition (Case 9) has a basic wave period $T = 5$ s and is plotted in Figure 2 (b). The formula is given in Appendix C. The skewed wave forcing velocity can be decomposed into two parts, the sharp phase, e.g., from $t = 5$ s to $t = 7$ s, and the gradual phase, e.g., from $t = 7$ s to $t = 10$ s. Generally, during more gradual deceleration phases, e.g., from $t = 12$ s to $t = 13.5$ s, some fast (i.e., 0.2 s) bursts of turbulence of characteristic thickness of 1 cm and turbulent kinetic energy level of approximately $2\text{x}10^{-3}$ m^2 s^{-2}, e.g., at $t = 13.5$ s, are present in Figure 14 (a). During sharp acceleration phases, the turbulent boundary layer response lasts about 1 s and has characteristic thickness of 0.5 cm and turbulent kinetic energy level of approximately $8\text{x}10^{-4}$ m^2 s^{-2}. A pattern of strong-weak-strong-weak turbulence can be observed. It is, however, interrupted by anomalous stronger turbulent bursts at $t = 15$ s and $t = 40$ s, i.e., every four wave periods. After these stronger bursts, the following wave periods exhibit weaker turbulence.

By calculating the acceleration of the flow, $a = \dfrac{\partial U_\infty(t)}{\partial t}$, plotted in Figure 15 (a), it can be observed that during gradual phases, the deceleration of the flow, which destabilizes the boundary layer, is relatively weak, i.e., 0.5 m s^{-2} and lasts 1.5 s, e.g., from $t = 7$ s to $t = 8.5$ s. During sharp phases, the deceleration of the flow is stronger, i.e., about 2.7 m s^{-2} and lasts only 0.5 s, e.g., from $t = 10.5$ s to $t = 11$ s.

The complex frequency wave (Case 10) is obtained by adding 5 sine waves with different amplitudes, frequencies, and phases; specifically

$$\begin{aligned} U_\infty(t) &= 0.2\sin(\frac{2\pi}{2}t + 1) + 0.3\sin(\frac{2\pi}{3}t + 34.9) + 0.3\sin(\frac{2\pi}{5}t + 1.6) + \\ &\quad 0.3\sin(\frac{2\pi}{7}t + 7) + 0.3\sin(\frac{2\pi}{11}t + 15) \text{ m s}^{-1}. \end{aligned} \tag{32}$$

The plot of the free stream velocity is shown in Figure 2 (c). The horizontally averaged turbulent kinetic energy for this complex wave forcing is given in Figure 14 (b). Significant turbulent bursts originate at approximately $t = 4.5$ s, $t = 8.5$ s, $t = 13.5$ s, $t = 21$ s, $t = 25.5$ s, and $t = 28$ s.

By considering the acceleration of the flow plotted in Figure 15 (b), these bursts occur shortly after periods of flow deceleration with magnitudes of about $a = 1.1$ m s^{-2}, $a = 1.5$ m s^{-2}, $a = 1.6$ m s^{-2}, $a = 1.2$ m s^{-2}, $a = 0.9$ m s^{-2}, and $a = 1.2$ m s^{-2}, respectively. Turbulent events do not occur for example at $t = 18$ s or $t = 23$ s during phases of flow deceleration with amplitudes of the order of $a = 0.2$ m s^{-2} and $a = 0.5$ m s^{-2}. For this experiment, whenever deceleration exceeds a threshold of approximately 0.8 m s^{-2}, the boundary layer becomes turbulent.

The wave packet (Case 11), product of two sine functions, is given by

$$U_\infty(t) = 0.8\sin(\frac{2\pi}{5}t)\sin(\frac{2\pi}{60}t) \text{ m s}^{-1}. \tag{33}$$

This represents a carrier wave with an envelope of 30 seconds modulating a higher frequency wave with period $T = 5$ s. The wave packet essentially groups several different

Reynolds number experiments together since U_m effectively changes over each short wave period of 5 s. Time series of the free-stream velocity are plotted in Figure 2 (d). The wave packet forcing condition induces corresponding packets of turbulence with a phase lag, as shown in Figure 14 (c). The boundary layer thickness, $\delta_\tau \approx 2$ cm, has the same basic shape as the carrier envelope. Clearly, the fundamental frequency of 5 seconds is evident in the bursts of turbulent kinetic energy. Asymmetry in the turbulent kinetic energy response is visible about the maximum of the envelope, which is centered at $t = 15$ s and $t = 45$ s. The turbulent kinetic energy has maximum between $17 < t < 20$ s and $47 < t < 49$ s, a phase lag of about 2-5 seconds or approximately one half to one wave period. This suggests that turbulence levels during preceding events influence the stability and production of turbulence during subsequent events. The periodicity of the turbulent kinetic energy, seen in Cases 1-4, is clearly evident for the case of the wave packet. The flow becomes turbulent at $t = 12.5$ s and 30 seconds later at $t = 42.5$ s when the free stream velocity $U_\infty(t)$ reaches a magnitude of 0.45 m s^{-1}. The turbulence decays when the magnitude of the velocity $U_\infty(t)$ again becomes too small, around $t = 28$ s and $t = 58$ s with $|U_\infty| < 0.3$ m s^{-1}. Correspondingly, it can be noticed in Figure 15 (c), that turbulence first develops when the deceleration of the flow is greater than $a = 0.95$ m s^{-2} and vanishes around $t = 28$ s when $a = 0.6$ m s^{-2}.

It can be concluded that different wave forms, i.e., different time-dependences of the free-stream velocity, especially near flow reversal, cause a different turbulent response in the boundary layer. The magnitude and the duration of the deceleration phases, and the recent history of the turbulence levels in the previous wave oscillations are important parameters in the generation of turbulence.

3.7 Combined Mean Flow and Wave Features

The final group of numerical experiments includes cross currents of different magnitudes in the y-direction, perpendicular to the direction of the wave oscillation. Characteristics of these wave-current flows (Cases 12-14) are described in Table 1.

3.7.1 Turbulent Kinetic Energy for Different Wave-Current Flows

The horizontally averaged turbulent kinetic energy for different mean currents, V_∞ = 0.15 m s^{-1} (Case 12), V_∞ = 0.30 m s^{-1} (Case 13) and V_∞ = 0.60 m s^{-1} (Case 14), superimposed upon a five-second period wave, $U_\infty = 0.60 \sin(\frac{2\pi}{5})$ m s^{-1}, are shown in Figures 16 (a), (b), and (c), respectively. These plots can be compared with Figure 11 (a), for $V_\infty = 0.0$ m s^{-1} (Case 2).

Addition of a weak mean current to the wave boundary layer can decrease the intensity of the turbulence. Figure 16 (a) shows significantly less turbulence than the case without any mean current, and the turbulence decreases with time. Figure 16 (a) produces an oscillatory wave flow with a weak drift. For panels (b) and (c), the addition of a mean current causes the boundary layer thickness to increase. In Case 14, the boundary layer thickness, δ_τ, can not be determined as it is simply larger than $L^{(z)}$. Most of the turbulent kinetic energy, however, is below 3 cm, with occasional eddies that hit the sponge layer. Flow visualizations suggest that the experiment represented in panel (c) is like a steady mean current with shifting direction and panel (b) is in an intermediate regime where, both, wave and steady flow features are present. The Reynolds number, in these cases, is determined with a maximum velocity amplitude $(U_m^2 + V_\infty^2)^{1/2}$. In panel (c), there is a discernible wave pulse in the turbulent kinetic energy related to wave flow reversal. Some qualitative similarities to the steady-flow case, Figure 13 (c), can be observed. The initial transition to turbulence for panels (a) and (b) occurs at $t = 5$ s, right at flow reversal. For panel (c), however, transition occurs at $t = 2.5$ s. This is

probably related to stronger instability associated with the stronger mean current. For $V_\infty = 0.30$ m s^{-1}, the turbulence does not completely extinguish between wave cycles compared to Cases 1 or 2 (i.e., at similar Re). This must be caused by the influence of the mean flow and continuous turbulent production in the y-direction.

3.7.2 Wall Shear Components for Different Mean Currents

Horizontally averaged wall shear components in the x-direction, τ_{xw}, and in the y-direction, τ_{yw}, as well as the root mean squared variances σ_{xw} and σ_{yw} are shown for different strengths of mean currents for combined wave-current experiments, $V_\infty = 0.0$ m s^{-1} (Case 2), $V_\infty = 0.15$ m s^{-1} (Case 12), $V_\infty = 0.30$ m s^{-1} (Case 13) and $V_\infty = 0.60$ m s^{-1} (Case 14) in Figure 17 (a), (b), (c) and (d), respectively. These quantities are given by

$$\tau_{xw} = \mu \left\langle \frac{\partial u}{\partial z}\Big|_w \right\rangle , \tag{34}$$

$$\tau_{yw} = \mu \left\langle \frac{\partial v}{\partial z}\Big|_w \right\rangle , \tag{35}$$

$$\sigma_{xw} = \mu \left\langle \left(\frac{\partial u}{\partial z}\Big|_w (x,y,t) - \left\langle \frac{\partial u}{\partial z}\Big|_w (t) \right\rangle \right)^2 \right\rangle^{1/2} , \tag{36}$$

$$\sigma_{yw} = \mu \left\langle \left(\frac{\partial v}{\partial z}\Big|_w (x,y,t) - \left\langle \frac{\partial v}{\partial z}\Big|_w (t) \right\rangle \right)^2 \right\rangle^{1/2} . \tag{37}$$

In panel (a), the u-component of the shear is almost periodic and sinusoidal and the variations from the horizontally mean wall shear, σ_{xw} and σ_{yw}, are small. In panel (a) and (c), $\sigma_{xw} > \sigma_{yw}$, which is a characteristic of the wave dominated situation, in panel (d), however, σ_{xw} is nearly equal to σ_{yw}, suggesting a more isotropic response during turbulence and that the flow, when $U_\infty = V_\infty$, is at a 45° angle. In panel (a), there is no mean shear in the y-direction. In panel (b), τ_{yw} decreases rapidly from $t = 0$ to $t = 5$ s from the value 0.2 Pa to 0.01 Pa, as the mean velocity profile adjusts from the initialized thin boundary layer profile. σ_{xw} and σ_{yw} are much smaller than in panel (a),

as this case is less turbulent, as seen in Figure 16 (a). In panels (c) and (d), it can be observed that as the current V_∞ increases, the y-component of the shear increases and its intensity fluctuates around 0.2 Pa and 0.4 Pa, respectively, for $V_\infty = 0.30$ m s^{-1} (Case 13) and $V_\infty = 0.60$ m s^{-1} (Case 14). Interestingly, τ_{yw} still decreases slowly with time. In Figure 17 (c), τ_{xw} is still periodic in time but is less like a sine wave than in Figure 17 (a). In Figure 17 (d), τ_{xw} increases to approximately 0.7-0.8 Pa compared to 0.6 Pa for panels (a), (b), and (c). For turbulent flows, the critical shear stress needed to suspend sediment of median grain size, d_{50}, on a flat horizontal surface is around 0.2 Pa for typical sand grains with diameters of approximately 0.2 mm [*Julien*, 1994]. The root mean squared variances increase as the mean currents and turbulence increase as shown in panels (c) and (d), suggesting that local wall shear stresses will significantly exceed mean values as turbulence levels increase, leading to increased potential for erosion of bed material (e.g., Figure 9).

3.8 Summary of the Experiments

Quantitative comparisons of average properties between the different numerical experiments conducted with the three-dimensional model are presented.

3.8.1 Turbulent Kinetic Energy and Kinetic Energy Dissipation Rates

Spatial and temporal means of the turbulent kinetic energy and the kinetic energy dissipation rate from the three-dimensional experiments are presented. These are compared to analytic results for laminar flows for different values of the wave period T, panels (a) and (b), different Reynolds numbers, panels (c) and (d), and different mean currents, V_∞, panels (e) and (f), in Figure 18.

The mean turbulent kinetic energy increases as the period T increases as shown in panel (a), consistent with the increase in boundary layer thickness with T. The mean turbulent kinetic energy varies as T increases by approximately a factor of 3 from $T = 5$ s

to $T = \infty$. The dissipation rate, plotted in panel (b), decreases as T increases for laminar flow but increases above the laminar results for the most turbulent cases, $T = 12.5$ s (Case 7) and $T = \infty$ (Case 8), in the three-dimensional model.

The mean turbulent kinetic energy also increases as the Reynolds number increases, for fixed $T = 5$ s, as shown in Figure 18 (c). The dissipation rate, panel (d), also increases for both the laminar and three-dimensional models as the Reynolds number increases. The three-dimensional results is slightly higher than the laminar result. The reason these values can be so similar in this intermittently turbulent regime is that the largest contribution to $\langle\langle\varepsilon\rangle\rangle$ comes from $\left\langle\left\langle\dfrac{\partial u}{\partial z}\right\rangle\right\rangle$ as shown in Figure 12.

Figure 18 (e) shows a point of inflection of the turbulent kinetic energy at $V_\infty = 0.15$ m s^{-1}, this case being less turbulent than the others. Generally, as the current V_∞ increases, the turbulent kinetic energy and dissipation rates increase, as shown in Figures 18 (e) and (f).

3.8.2 Friction Coefficient

Two friction coefficients are calculated for various three-dimensional experiments, C_{fm}, based on maximum values of the horizontally averaged wall shear, $\langle\langle\tau_{wm}\rangle\rangle$, and the maximum velocity amplitude, U,

$$C_{fm} = \frac{\langle\langle\tau_{wm}\rangle\rangle}{\frac{1}{2}\rho U^2}, \tag{38}$$

and $\overline{C_f}$ based on time average values of the horizontally averaged wall shear, $\langle\langle\overline{\tau_w}\rangle\rangle$, and the mean velocity amplitude, $\overline{U_\infty}$,

$$\overline{C_f} = \frac{\langle\langle\overline{\tau_w}\rangle\rangle}{\frac{1}{2}\rho\overline{U}^2}. \tag{39}$$

In these equations, the velocity amplitudes are $U = (U_m^2 + V_\infty^2)^{1/2}$, $\overline{U} = (\overline{U_\infty}^2 + V_\infty^2)^{1/2}$, and the wall shears $\langle\langle\tau_{wm}\rangle\rangle = (\langle\langle\tau_{xwm}\rangle\rangle^2 + \langle\langle\tau_{ywm}\rangle\rangle^2)^{1/2}$, $\langle\langle\overline{\tau_w}\rangle\rangle = (\langle\langle\overline{\tau_{xw}}\rangle\rangle^2 + \langle\langle\overline{\tau_{yw}}\rangle\rangle^2)^{1/2}$.

$\langle\langle\tau_{xwm}\rangle\rangle$ and $\langle\langle\tau_{ywm}\rangle\rangle$ are the maximum values over the wave cycle of the u- and v-components of the wall shear defined in equations (34) and (35), respectively, and $\overline{\tau_{xw}}$ and $\overline{\tau_{yw}}$ are the rms time averaged values of the u- and v-component of the wall shear.

Results are displayed in Tables 3 and 4 for different cases and are compared to the friction coefficient based on the maximum predicted shear at the wall, $f_w = \frac{2}{\sqrt{Re_\omega}}$, which is valid for smooth laminar flow, $Re_\omega < 3\text{x}10^5$ [*Nielsen*, 1992]. It can be observed that the results obtained from the three-dimensional simulations are of the same order of magnitude as those obtained for laminar flows. The friction coefficients are presented for different values of the wave period T, panel (a), different Reynolds numbers Re, panel (b), and different mean currents, V_∞, panel (c), in Figure 19. As the wave period increases (Cases 1, 5-7), panel (a), the u-component of the wall shear and the friction coefficients decrease from $T = 3$ to $T = 8$ s and then increases for $T = 12.5$ s, the velocity U being constant for this panel. The value of the friction coefficient based on time average values of the wall shear and free-stream velocity is larger than the friction coefficient based on maximum values since the shear is divided by the velocity squared. In panel (b) (Cases 1-4), the friction coefficients decrease as the Reynolds number (or the velocity U) increases. The friction coefficients also decrease and the shear at the wall increases as the mean current strength increases as shown in panel (c) (Case 2, 12-14). In summary, the friction coefficient decreases as the period, Reynolds number or current strength increase, that is as the flow becomes turbulent, which is in good agreement with the literature [*Kamphuis*, 1975; *Sleath*, 1987; *Jensen et al.*, 1989; and *Hino et al.*, 1989].

4 Summary

Numerical experiments have been conducted with the high-resolution time-dependent three-dimensional turbulent boundary layer model developed by *Slinn and Riley* [1998] in order to study the dynamics of the wave bottom boundary layer. Variations of free-stream velocities, similar to those common in nature, have been applied. The results have shown that the model can make direct estimates for wave energy dissipation rates and turbulent kinetic energy for turbulent boundary layers that occur near a smooth sea-bed. Simulations have presented the dependence of the boundary layer on surface wave field conditions (wave amplitude, wave frequency, wave shape, and presence of mean current) and described the different kinds of flow, laminar, transitional, and turbulent that are produced. Analysis of the basic flow features for a five-second period wave of maximum amplitude 0.80 m s^{-1} has shown that the turbulence in the wave bottom boundary layer depicts initial transients during the first two wave periods before achieving a quasi-steady behavior. Subsequently, turbulent bursts become episodic in nature and are coupled to the wave cycle. Accelerating flow organizes the boundary layer structure, and decelerating flow destabilizes the boundary layer. Turbulent levels are usually the strongest near flow reversal. Moreover, the decay of turbulence seems to be more rapid than the onset of turbulence. Analysis of the kinetic energy dissipation rates has shown that the model is sufficiently well-resolved and that the spatial resolution used in the three-dimensional model is adequate to the purposes of this work as the grid spacing is on the order of the Kolmogorov length scale.

The model has been tested for different Reynolds numbers based on $Re = \dfrac{U_m L^{(z)}}{\nu}$, by varying the wave amplitude, U_m, and holding the wave period fixed. As the wave amplitude decreases, the turbulent kinetic energy and the turbulent boundary layer thickness decrease. A significant factor is that the magnitude of the deceleration of the

wave forcing decreases as the wave amplitude decreases. For a maximum current velocity less than about 40 cm s^{-1} the flow remains laminar. The laminar to turbulent transition occurs in the model for $Re \sim 25{,}000$ or $Re_\omega \sim 100{,}000$, which is in good agreement with previous laboratory experiments [*Jonsson*, 1980].

Results of numerical experiments that varied the wave period, T, show that as the wave period increases, the boundary layer thickness increases and the flow becomes more turbulent, with steady flow being the most turbulent. As the magnitude of the acceleration-deceleration phases decreases as the wave period increases, it is suggested that the duration of the deceleration phase can be more significant than its amplitude for some flow situations.

Different shapes of wave forcing conditions (e.g., skewed wave, complex frequency wave, and wave packet) have also been examined to understand the dynamics at flow reversal. It has been concluded that the magnitude of the deceleration, the duration of the deceleration phase, the Stokes layer thickness, and the recent history of the flow during preceding wave periods are important parameters in the production and intensity of the turbulent events.

Finally, mean currents of various amplitudes, perpendicular to the direction of wave oscillation, have been added to the model. The impact of a weak current ($V_\infty \sim 0.25U_m$) is to reduce the turbulence produced by the wave motion. The addition of a relatively strong current ($V_\infty > 0.5U_m$) results in increasingly turbulent flows as V_∞ increased.

Generally, the dissipation rate increases when the turbulent kinetic energy increases, as the wave period, the wave amplitude or current strength increase. Finally, friction coefficients have been calculated for different experiments and have been found to decrease as the flow becomes more turbulent and to be of the same order of magnitude as those given previously in the literature.

Acknowledgements. This work was supported by the Office of Naval Research, Physical Oceanography Program, as part of the Shoaling Wave Experiment under Grant Number N00014-99-1-0065.

References

Akhavan, R., Kamm, R. D., Shapiro, A. H., An investigation of transition to turbulence in bounded oscillatory Stokes flows, Part 2: Numerical simulations, *J. Fluid Mech.*, 255, 423-444, 1991.

Asano, T., Iwagaki, Y., Bottom boundary layer in wave-current co-existing systems, *Proc. 19th Conf. Coastal Eng.*, 2397-2413, 1984.

Asano, T., Nakagawa, M., Iwagaki, Y., Changes in current properties due to wave superimposing, *Proc. 20th Conf. Coastal Eng.*, 925-939, 1986.

Bakker, W. T., Van Doorn, T., Turbulent currents in the presence of waves, *Proc. 14th Conf. Coastal Eng.*, 1129-1148, 1978a.

Bakker, W. T., Van Doorn, T., Near-bottom velocities in wave with a current, *Proc. 16th Conf. Coastal Eng.*, 1394-1413, 1978b.

Barrantes, A. I., Madsen, O. S., Near-bottom flow and flow resistance for currents obliquely incident to two-dimensional roughness elements, *J. Geophys. Res.*, 105, 26,253-26,264, 2000.

Batchelor, G. K., *An introduction to fluid dynamics*, 615 pp., Cambridge University Press, Cambridge, 1967.

Bijker, E. W., The increase of bed shear in a current due to wave motion, *Proc. 10th Conf. Coastal Eng.*, 746-765, 1966.

Blondeaux, P., Sand ripples under sea waves, Part 1: Ripple formation, *J. Fluid Mech.*, 264, 107-135, 1990.

Canuto C., Hussaini, M. Y., Quarteroni, A., Zang, T. A., *Spectral methods in fluid dynamics*, 557 pp., Springer Verlag, New York, 1988.

Christoffersen, J. B., Jonsson, I. G., Bed friction and dissipation in a combined current and wave motion, *Ocean Eng.*, 12, 387-423, 1985.

Coffey, F. C., Nielsen, P., Aspects of wave current boundary layer flows, *Proc. 19th Conf. Coastal Eng.*, 2232-2245, 1984.

Coffey, F. C., Nielsen, P., The influence of waves on current profiles, *Proc. 20th Conf. Coastal Eng.*, 82-96, 1986.

Davies, A. G., Soulsby, R. L., King, H. L., A numerical model of the combined wave and current bottom boundary layer, *J. Geophys. Res.*, 93, 491-508, 1988.

Davies, A. G., Ribberink, J. S., Temperville, A., Zyserman, J. A., Comparisons between sediment transport models and observations made in wave and current flows above plane

beds, *Coastal Eng.*, 31, 163-198, 1997.

Dean, R. G., Dalrymple, R. A., *Water wave mechanics for engineers and scientists*, 353 pp., Advanced series on ocean engineering, Volume 2, World Scientific, 1991.

Dick, J. E., Erdman, M. R., Hanes, D. M., Suspended sand concentration events due to shoaled waves over a flat bed, *Mar. Geol.*, 119, 67-73, 1994.

Durran, D. R., Yang, M. Z., Slinn, D. N., Brown, R., Towards more accurate wave-permeable boundary conditions, *Monthly Weather Rev.*, 121, 604-620, 1993.

Dyer, K. R., Soulsby, R. L., Sand transport on the continental shelf, *Ann. Rev. Fluid Mech.*, 20, 295-324, 1988.

Feddersen, F., Guza, R. T., Velocity moments in longshore bottom stress parameterizations, *J. Geophys. Res.*, 105, 8673-8686, 2000.

Foster, D. L., Holman, R. A., Beach, R. A., Sediment suspension events and shear instabilities in the bottom boundary layer, *Coastal Dynamics*, 712-726, 1994.

Foster, D. L., Beach, R. A., Holman, R. A., Field observations of the wave bottom boundary layer, *J. Geophys. Res.*, 105, 19,631-19,647, 2000.

Fredsoe, J., Turbulent boundary layer in wave-current motion, *J. Hydraul. Eng.*, 110, 1103-1120, 1984.

Fredsoe, J., Deigaard, R., *Mechanics of coastal sediment transport*, 369 pp., Advanced series on ocean engineering, Volume 3, World Scientific, 1992.

Fredsoe, J., Andersen, K. H., Sumer, B. M., Wave plus current over a ripple-covered bed, *Coastal Eng.*, 38, 177-221, 1999.

Gad-El-Hak, M., Davis, S. H., McMurray, J. T., Orszag, S. A., On the stability of the decelerating laminar boundary layer, *J. Fluid Mech.*, 138, 297-323, 1984.

Garcez Faria, A. F., Thornton, E. B., Stanton, T. P., Soares, C. V., Vertical profiles of longshore currents and related bed shear stress and bottom roughness, *J. Geophys. Res.*, 103, 3217-3232, 1998.

Grant, W. D., Madsen, O. S., Combined wave and current interaction with a rough bottom, *J. Geophys. Res.*, 84, 1797-1808, 1979.

Grant, W. D., Williams, A. J., III, Glenn, S. M., Bottom stress estimates and their prediction on the northern California continental shelf during CODE-1: The importance of wave-current interaction, *J. Phys. Oceanogr.*, 14, 506-527, 1984.

Grant, W. D., Madsen, O. S., The continental-shelf bottom boundary layer, *Ann. Rev. Fluid Mech.*, 18, 265-305, 1986.

Hanes, D. M., Huntley, D. A., Continuous measurements of suspended sand concentration in a wave dominated nearshore environment, *Cont. Shelf Res.*, 6, 585-596, 1986.

Hanes, D. M., Intermittent sediment suspension and its implications to sand tracer dispersal in wave-dominated environments, *Mar. Geol.*, 88, 175-183, 1988.

Hay, A. E., Bowen, A. J., Coherence scales of wave-induced suspended sand concentration fluctuations, *J. Geophys. Res.*, 99, 12,749-12,765, 1994.

Hino, M., Kashiwayanagi, M., Nakayama, A. Hara, T., Experiments on the turbulence statistics and the structure of a reciprocating oscillatory flow, *J. Fluid Mech.*, 206, 265-297, 1989.

Houwman, K. T., Van Rijn, L. C., Technical note, Flow resistance in the coastal zone, *Coastal Eng.*, 38, 261-273, 1999.

Huntley, D. A., Hazen, D. G., Seabed stresses in combined wave and steady flow conditions on the Nova Scotia continental shelf: Field measurements and predictions, *J. Phys. Oceanogr.*, 18, 347-362, 1988.

Jensen, B., L., Sumer, B. M., Fredsoe, J., Turbulent oscillatory boundary layers at high Reynolds numbers, *J. Fluid Mech.*, 206, 265-297, 1989.

Johns, B., Residual flow and boundary shear stress in the turbulent bottom boundary layer beneath waves, *J. Phys. Oceanogr.*, 7, 733-738, 1977.

Jonsson, I. G., Carlsen, N., A., Experimental and theoretical investigations in an oscillatory turbulent boundary layer, *J. Hydraul. Res.*, 14, 45-60, 1976.

Jonsson, I. G., A new approach to oscillatory rough turbulent boundary layer, *Ocean Eng.*, 7, 109-152, 1980.

Julien, P. Y., *Erosion and sedimentation*, 298 pp., Cambridge University Press, 1994.

Justesen, P., Prediction of turbulent oscillatory flow over rough bed, *Ocean Eng.*, 12, 257-284, 1988.

Kamphuis, J. W., Friction factor under oscillatory waves, *J. Waterways, Harbors and Coastal Eng. Div.*, 101, 135-144, 1975.

Kemp, P. H., Simons, R. R., The interaction between waves and a turbulent current: Waves propagating with the current, *J. Fluid Mech.*, 116, 227-250, 1982.

Kemp, P. H., Simons, R. R., The interaction between waves and a turbulent current: Waves propagating against the current, *J. Fluid Mech.*, 130, 73-89, 1983.

Lambrakos, K. F., Myrhaug, D, Slaattelid, O. H., Seabed current boundary layers in wave-plus-current flow combinations, *J. Waterway, Port, Coastal and Ocean Div.*, 114,

161-174, 1988.

Lele, S. K., Compact finite difference schemes with spectral-like resolution, *J. Comput. Phys.*, 103, 16, 1992.

Li, M. Z., Amos, C. L., Predicting ripple geometry and bed roughness under combined waves and currents in a continental shelf environment, *Cont. Shelf Res.*, 18, 941-970, 1998.

Liu, P. L. F, Dalrymple, R. A., Bottom frictional stresses and longshore currents due to waves with large angle of incidence, *J. Mar. Res.*, 36, 359-375, 1978.

Lundgren, H., Turbulent currents in the presence of waves, *Proc. 13th Conf. Coastal Eng.*, 1, 623-634, 1972.

Mathisen, P. P., Madsen, O. S., Waves and currents over a fixed rippled bed 3. Bottom and apparent roughness for spectral waves and currents, *J. Geophys. Res.*, 104, 18,447-18,461, 1999.

Mei, C. C., *The applied dynamics of ocean surface waves*, 768 pp., Advanced series on ocean engineering, Volume 1, World Scientific, 1989.

Moin, P., Mahesh, K., Direct numerical simulation: A tool in turbulence research, *Ann. Rev. Fluid Mech.*, 30, 539-578, 1998.

Myrhaug, D., On a theoretical model of rough turbulent wave boundary layers, *Ocean Eng.*, 9, 547-565, 1982.

Myrhaug, D., Slaattelid, O. H., Combined wave and current boundary layer model for fixed rough seabeds, *Ocean Eng.*, 16, 119-142, 1989.

Myrhaug, D., Slaattelid, O. H., A rational approach to wave-current friction coefficients for rough, smooth and transitional turbulent flow, *Coastal Eng.*, 14, 265-293, 1990.

Nielsen, P., *Coastal bottom boundary layers and sediment transport*, 324 pp., Advanced series on ocean engineering, Volume 4, World Scientific, 1992.

O'Connor, B. A., Yoo, D., Mean bed friction of combined wave/current flow, *Coastal Eng.*, 12, 1-21, 1988.

Panton, R. L., The transient for Stokes's oscillating plate: A solution in terms of tabulated functions, *J. Fluid Mech.*, 31, 4, 819-825, 1968.

Piomelli, U., Balaras, E., Pascarelli, A., Turbulent structures in accelerating boundary layers, *J. Turb.*, 2000.

Rankin, K. L., Hires, R. I., Laboratory measurements of bottom shear stress on a movable bed, *J. Geophys. Res.*, 105, 17,011-17,019, 2000.

Ribberink, J. S., Al-Salem, A. A., Sediment transport in oscillatory boundary layers in cases of rippled beds and sheet flow, *J. Geophys. Res.*, 99, 12,707-12,727, 1994.

Sarpkaya, T., Coherent structures in oscillatory boundary layers, *J. Fluid Mech.*, 253, 105-140, 1993.

Schlichting, H., *Boundary layer theory*, 4^{th} ed., 647 pp., McGraw-Hill, New York, 1968.

Sleath, J. F. A., Turbulent oscillatory flow over rough beds, *J. Fluid Mech.*, 182, 369-409, 1987.

Sleath, J. F. A., Transition in oscillatory flow over rough beds, *J. Waterway, Port, Coastal, and Ocean Div.*, 114, 18-33, 1988.

Sleath, J. F. A., Bed friction and velocity distributions in combined steady and oscillatory flow, *Proc. 22^{nd} Conf. Coastal Eng.*, 450-463, 1990.

Sleath, J. F. A., Velocities and shear stresses in wave-current flows, *J. Geophys. Res.*, 96, 15,237-15,244, 1991.

Slinn, D. N., Riley, J. J., A model for the simulation of turbulent boundary layers in an incompressible stratified flow, *J. Comput. Phys.*, 144, 550-602, 1998.

Smith, J. D., Modeling of sediment transport on continental shelves, *The Sea*, 6, 539-577, 1977.

Soulsby, R. L., Hamm, L., Klopman, G., Myrhaug, D., Simons, R. R., Thomas, G. P., Wave-current interaction within and outside the bottom boundary layer, *Coastal Eng.*, 21, 41-69, 1993.

Spalart, P. R., Baldwin, B. S., Direct simulation of a turbulent oscillating boundary layer, *Tech. Memo.*, 89460, 1987.

Spalart, P., Direct numerical simulation of a turbulent boundary layer up to $R_\theta = 1410$, *J. Fluid Mech.*, 187, 61-98, 1988.

Staub, C., Jonsson, I. G., Svendsen, I. A., Sediment suspension in oscillatory flow: Measurements of instantaneous concentration at high shear, *Coastal Eng.*, 27, 67-96, 1996.

Stokes, G. G., On the theories of the internal friction of fluids in motion, *Trans. Camb. Phil. Soc.*, 8, 287, 1845.

Tennekes, H., Lumley, J. L., *A first course in turbulence*, MIT Press, Cambridge, Mass, 1972.

Trowbridge, J., Madsen, O. S., Turbulent wave boundary layers 1. Model formulation and first-order solution, *J. Geophys. Res.*, 89, 7989-7997, 1984.

Trowbridge, J. H., Agraval, Y. C., Glimpses of a wave boundary layer, *J. Geophys. Res.*,

100, 20,729-20,743, 1995.

Van Doorn, T., Experimental investigation of near bottom velocities in water waves with and without a current, *TOW-Report*, 1981.

Van Kesteren, W. G. M., Bakker, W. T., Near bottom velocities in waves with a current; Analytical and numerical computations, *Proc. 19th Conf. Coastal Eng.*, 1161-1177, 1984.

Vittori, G., Verzicco, R., Direct simulation of transition in Stokes boundary layers, *J. Fluid Mech.*, 371, 207-232, 1998.

Yang, K. S., Spalart, P. R., Ferziger, J. H., Numerical studies of natural transition in a decelerating boundary layer, *J. Fluid Mech.*, 240, 433-468, 1992.

Zhao, Y., Anastasiou, K., Bottom friction effects in the combined flow field of random waves and currents, *Ocean Eng.*, 19, 223-243, 1993.

Appendix A: Kinetic Energy Spectra

The kinetic energy spectra and its three components u^2, v^2, and w^2, are calculated using Fast Fourier Transforms of $u(x, y, z, t_0)$, $v(x, y, z, t_0)$, and $w(x, y, z, t_0)$ in the along-stream or cross-stream directions. Assuming Fourier component wave solutions for the variables u, v, and w of the form $u(x) = \hat{u}(k_x)e^{ik_x}$ in the x-direction or $u(y) = \hat{u}(k_y)e^{ik_y}$ in the y-direction, and periodicity in x with period $L^{(x)}$ and in y with period $L^{(y)}$, the fields can be expanded in truncated Fourier series with corresponding Fourier coefficients, for example in the streamwise direction,

$$\hat{u}(k_x(n)) = \frac{1}{N}\sum_{i=0}^{N-1} u(x_i)e^{-ik_x(n)x_i}, \qquad (A1)$$

where $x_i = L^{(x)}i/N$, $i = 0, 1, \ldots, N$-1 and $k_x(n)$ are the wavenumbers given by $2\pi n/L^{(x)}$. The mode numbers n range from $n = 0, 1, \ldots, N$-1 where N is the total number of grid points in x, i.e., 256 [*Canuto et al.*, 1988]. Thus, the kinetic energy is defined as a function of the alongshore wavenumbers k_x with

$$KE(k_x) = \frac{1}{2}\big[\hat{u}(k_x(n))\hat{u}^*(k_x(n)) + \hat{v}(k_x(n))\hat{v}^*(k_x(n)) + \hat{w}(k_x(n))\hat{w}^*(k_x(n))\big], \qquad (A2)$$

where $\hat{u}^*$, $\hat{v}^*$, and $\hat{w}^*$ are the complex conjugates of $\hat{u}$, $\hat{v}$, and $\hat{w}$, respectively.

Appendix B: Numerical Resolutions

A common problem exists if the physical flow being simulated produces smaller energy containing eddies than can be well represented in the model. Generally, turbulence produces a cascade of energy towards smaller scales that continue down to the Kolmogorov length-scale at which viscosity dominates inertial effects and energy dissipation is completed. According to *Moin and Mahesh* [1998], the smallest resolved length scale is required to be of the order of η, where η is the Kolmogorov length scale defined by

$$\eta = \left(\frac{\nu^3}{\varepsilon}\right)^{1/4}, \tag{40}$$

where ε is the kinetic energy dissipation rate and ν the kinematic viscosity. Using the mean value for the dissipation rate, $\langle\langle\varepsilon\rangle\rangle = 6$ W m^{-3}/1000 kg m^{-3}, the Kolmogorov length-scale becomes in this problem

$$\eta = \left(\frac{1000(10^{-6})^3}{6}\right)^{1/4} \approx 0.12 \quad \text{mm}. \tag{41}$$

For this case, the grid resolution is $\Delta x = 0.4$ mm, $\Delta y = 0.6$ mm, and $\Delta z = 0.1$ mm in the x-, y-, and z-direction, using the value of Δz near the wall. For the steady flow boundary layer, *Spalart* [1988] conducted direct numerical simulation studies using a resolution of

$$\Delta x = 14.3\eta, \qquad \Delta y = 4.8\eta, \qquad \Delta z = 0.33\eta. \tag{42}$$

The resolution used in the three-dimensional numerical simulations in this work are

$$\Delta x = 3.3\eta, \qquad \Delta y = 5\eta, \qquad \Delta z = 0.83\eta. \tag{43}$$

The spatial resolution used in the three-dimensional model appears adequate for the purposes of this work as the grid spacing is of the order of the Kolmogorov length scale and similar to that used in previous related work.

Appendix C: Skewed Wave Velocity

The skewed wave forcing condition is given by

$$U_\infty(t) = -0.8(U_{free} - 4.0), \tag{B1}$$

where U_{free} is determined iteratively using

$$U_{free} = 4.0 + \sin\left[\frac{2\pi}{5}\left(t - \frac{C}{U_{old}^2}\right)\right], \tag{B2}$$

where $C = 18$ is a constant and U_{old} equals the value of U_{free} at a previous iteration. The value of U_{free} is obtained by iteration, i.e., by substituting U_{old} by the previous value of U_{free} till the difference between U_{free} and U_{old} is less than 10^{-10}.

Cases	U_m, V_∞ (m s^{-1})	T (s)	δ_s (cm)	δ_τ (cm)	Re $\frac{U_m L^{(z)}}{\nu}$	Re_ω $\frac{U_m^2 T}{2\pi\nu}$	Re_{δ_τ} $\frac{U_m \delta_\tau}{\nu}$	$Re_{\delta s}$ $U_m\sqrt{\frac{T}{\nu\pi}}$
1	0.80, 0.0	5	0.13	2.0	40,000	510,000	16,000	1,009
2	0.60, 0.0	5	0.13	1.0	30,000	290,000	6,000	757
3	0.40, 0.0	5	0.13	0.13	20,000	130,000	504	504
4	0.20, 0.0	5	0.13	0.13	10,000	32,000	252	252
5	0.80, 0.0	3	0.097	0.5	40,000	300,000	4,000	782
6	0.80, 0.0	8	2.5	0.16	40,000	815,000	20,000	1,277
7	0.80, 0.0	12.5	0.2	3.0	40,000	1,270,000	24,000	1,596
8	0.80, 0.0	∞	-	4.0	40,000	∞	32,000	∞
9	0.80, 0.0	Skewed	-	2.5	40,000	510,000	20,000	1,009
10	1.00, 0.0	Complex	-	1.2	50,000	-	12,000	1,009
11	0.80, 0.0	Packet	-	2.0	40,000	-	16,000	3,497
12	0.60, 0.15	5	-	0.6	31,000	307,000	3,700	782
13	0.60, 0.30	5	-	2.5	33,500	530,000	16,700	845
14	0.60, 0.60	5	-	4.5	42,000	575,000	37,800	1060

Table 1: Characteristics of the different three-dimensional experiments: maximum free-stream velocity amplitude, U_m; current strength, V_∞; period, T; Stokes boundary layer thickness, δ_s; turbulent boundary layer thickness, δ_τ; and Reynolds numbers based on amplitude, Re; frequency, Re_ω; turbulent boundary layer thickness, Re_{δ_τ}; and Stokes boundary layer thickness, $Re_{\delta s}$. Note that for laminar flows (Cases 3-4), δ_s is used for δ_τ.

T (s)	3	5	5	8	8	12.5	12.5
h (m)	3	3	15	3	15	3	15
λ (m)	12.68	24.93	38.46	42.03	81.79	66.94	141.83
H (m)	1.60	1.06	7.33	0.94	2.90	0.91	2.27
$u_{z=0}$ (m s^{-1})	1.86	1.04	4.67	0.88	1.39	0.83	0.98
$\tanh(kh)$	0.90	0.64	0.99	0.42	0.82	0.27	0.58

Table 2: Characteristics of the different wave flows: wave period, T; water depth, h; wavelength, λ; wave height, H; maximum velocity at the surface, $u_{z=0}$; with a boundary layer velocity, $u_{z=-h} = 0.80$ m s^{-1}.

Cases	$\langle\langle\tau_{xwm}\rangle\rangle$ (Pa)	$\langle\langle\tau_{ywm}\rangle\rangle$ (Pa)	$\langle\langle\tau_{wm}\rangle\rangle$ (Pa)	U_m (m s^{-1})	V_∞ (m s^{-1})	U $\sqrt{U_m^2+V_\infty^2}$ (m s^{-1})	C_{fm} $\frac{\langle\langle\tau_{wm}\rangle\rangle}{\frac{1}{2}\rho U^2}$	f_w $\frac{2}{\sqrt{Re_\omega}}$
1	0.818	0.02	0.818	0.80	0.00	0.80	0.0026	0.0028
2	0.667	0.00	0.667	0.60	0.00	0.60	0.0037	0.0037
3	0.444	0.00	0.444	0.40	0.00	0.40	0.0056	0.0055
4	0.222	0.00	0.222	0.20	0.00	0.20	0.0111	0.0112
5	1.135	0.00	1.135	0.80	0.00	0.80	0.0035	0.0037
6	0.655	0.00	0.655	0.80	0.00	0.80	0.0020	0.0022
7	1.122	0.00	1.122	0.80	0.00	0.80	0.0035	0.0018
12	0.666	0.150	0.682	0.60	0.15	0.618	0.0036	0.0036
13	0.678	0.256	0.725	0.60	0.30	0.671	0.0032	0.0027
14	0.869	0.576	1.043	0.60	0.60	0.848	0.0029	0.0026

Table 3: Friction coefficient based on maximum values of wall shear and free stream velocity.

Cases	$\langle\langle\overline{\tau_{xw}}\rangle\rangle$ (Pa)	$\langle\langle\overline{\tau_{yw}}\rangle\rangle$ (Pa)	$\langle\langle\overline{\tau_w}\rangle\rangle$ (Pa)	$\overline{U_\infty}$ (m s^{-1})	V_∞ (m s^{-1})	$\overline{U}$ $\sqrt{\overline{U_\infty}^2+V_\infty^2}$ (m s^{-1})	$\overline{C_f}$ $\frac{\langle\langle\overline{\tau_w}\rangle\rangle}{\frac{1}{2}\rho\overline{U}^2}$
1	0.498	0.0046	0.498	0.509	0.00	0.509	0.0038
2	0.390	0.00128	0.390	0.382	0.00	0.382	0.0053
3	0.268	0.00	0.268	0.255	0.00	0.255	0.0083
4	0.135	0.00	0.135	0.128	0.00	0.127	0.0167
5	0.691	0.0002	0.691	0.509	0.00	0.509	0.0053
6	0.396	0.0009	0.396	0.509	0.00	0.509	0.0031
7	0.560	0.0051	0.560	0.509	0.00	0.509	0.0043
12	0.410	0.030	0.411	0.382	0.15	0.410	0.0049
13	0.383	0.152	0.412	0.382	0.30	0.486	0.0035
14	0.488	0.401	0.632	0.382	0.60	0.711	0.0025

Table 4: Friction coefficient based on time average of wall shear and free stream velocity.

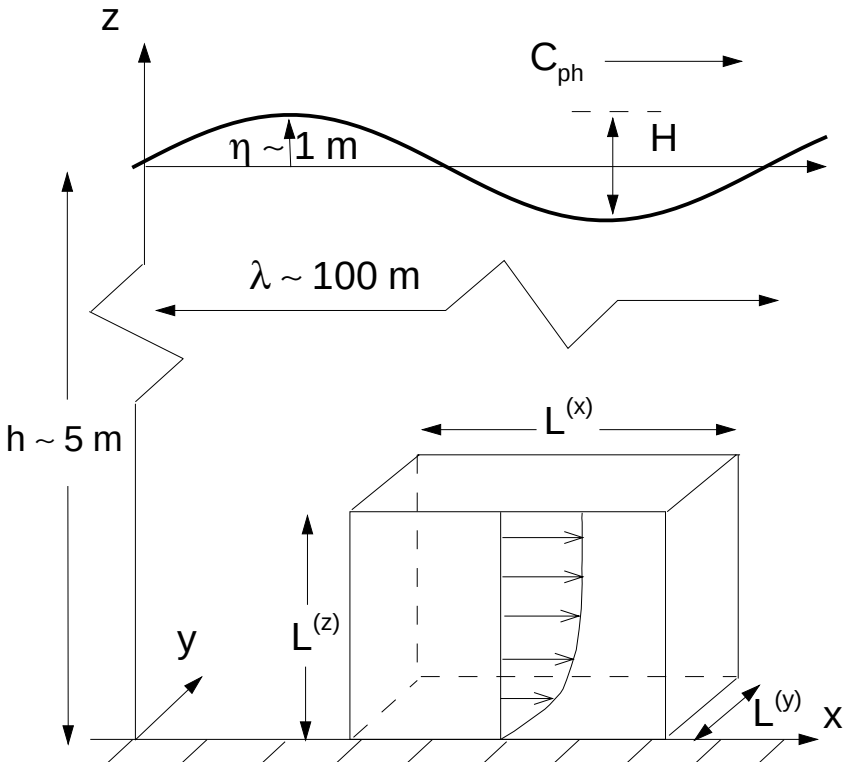

Figure 1: Horizontally periodic boundary layer domain (dimensions of the order of 10 cm^3) under a progressive wave of height H, wavelength λ, and water depth h.

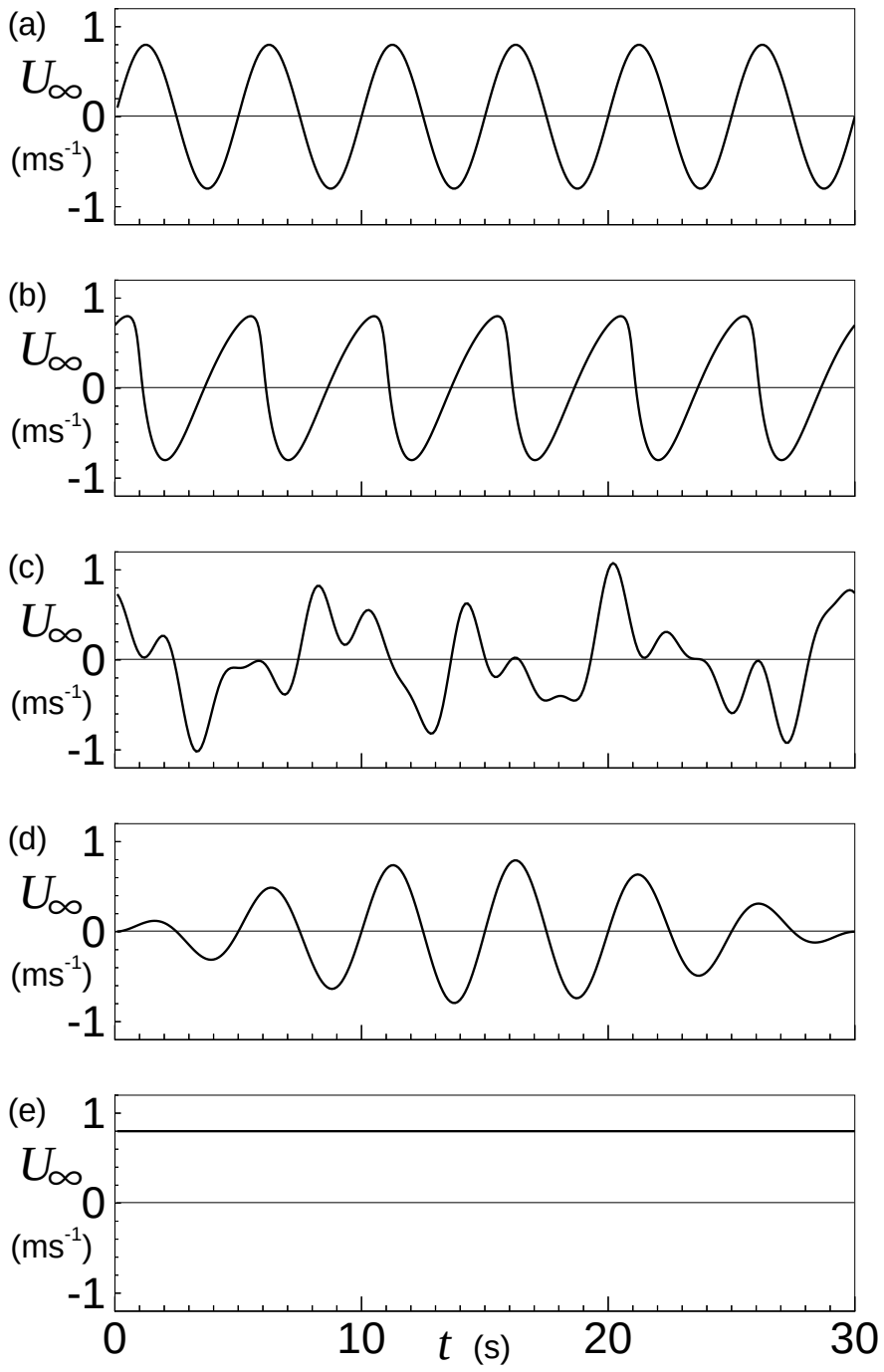

Figure 2: Forcing time series of free stream velocity, U_∞, for different experiments: (a) sine wave; (b) skewed wave; (c) complex frequency wave; (d) wave packet; and (e) steady flow.

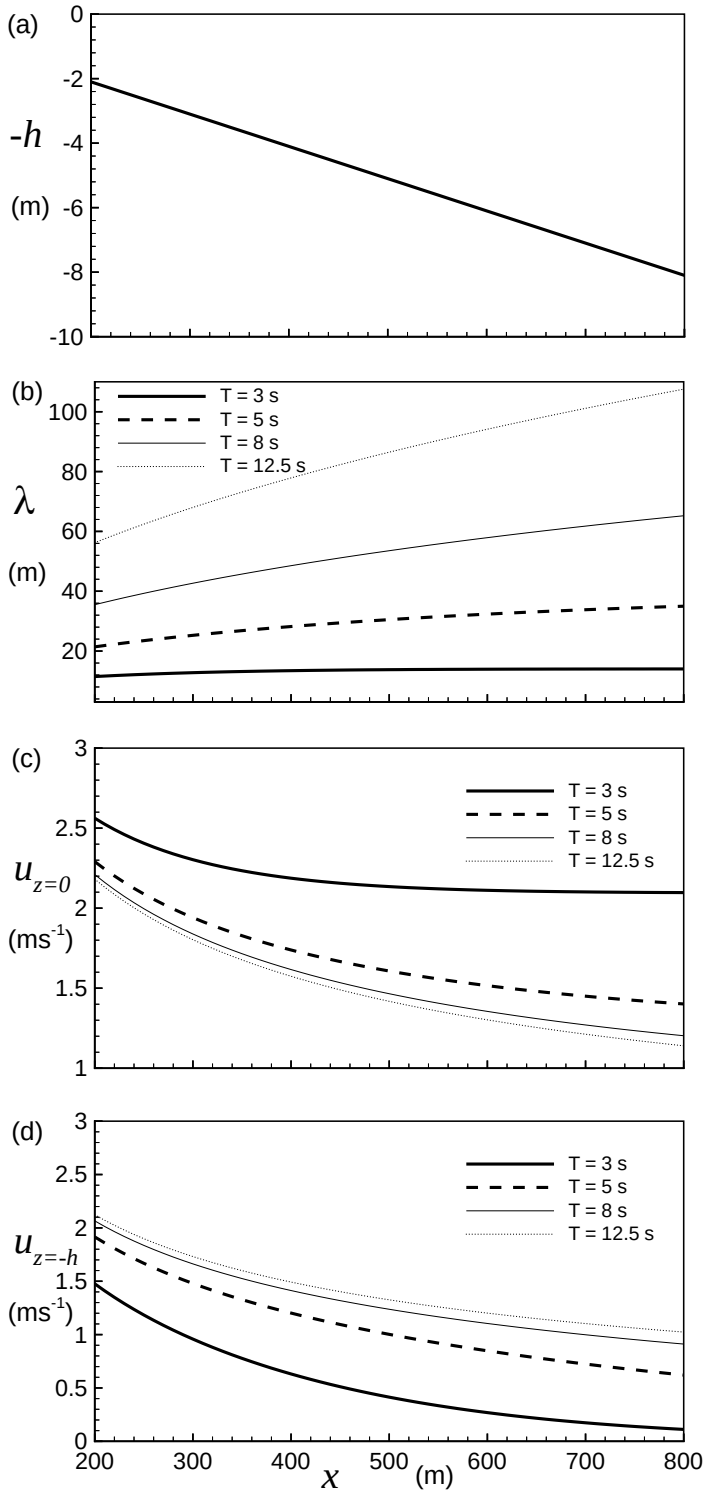

Figure 3: For a wave height $H = 2$ m over (a) water depth, h, with a 1% slope; (b) wavelength, λ; (c) maximum wave velocity, $u_{z=0}$; (d) wave induced velocity just above the bottom boundary layer, $u_{z=-h}$; as a function of distance from the shore x, for different wave periods T.

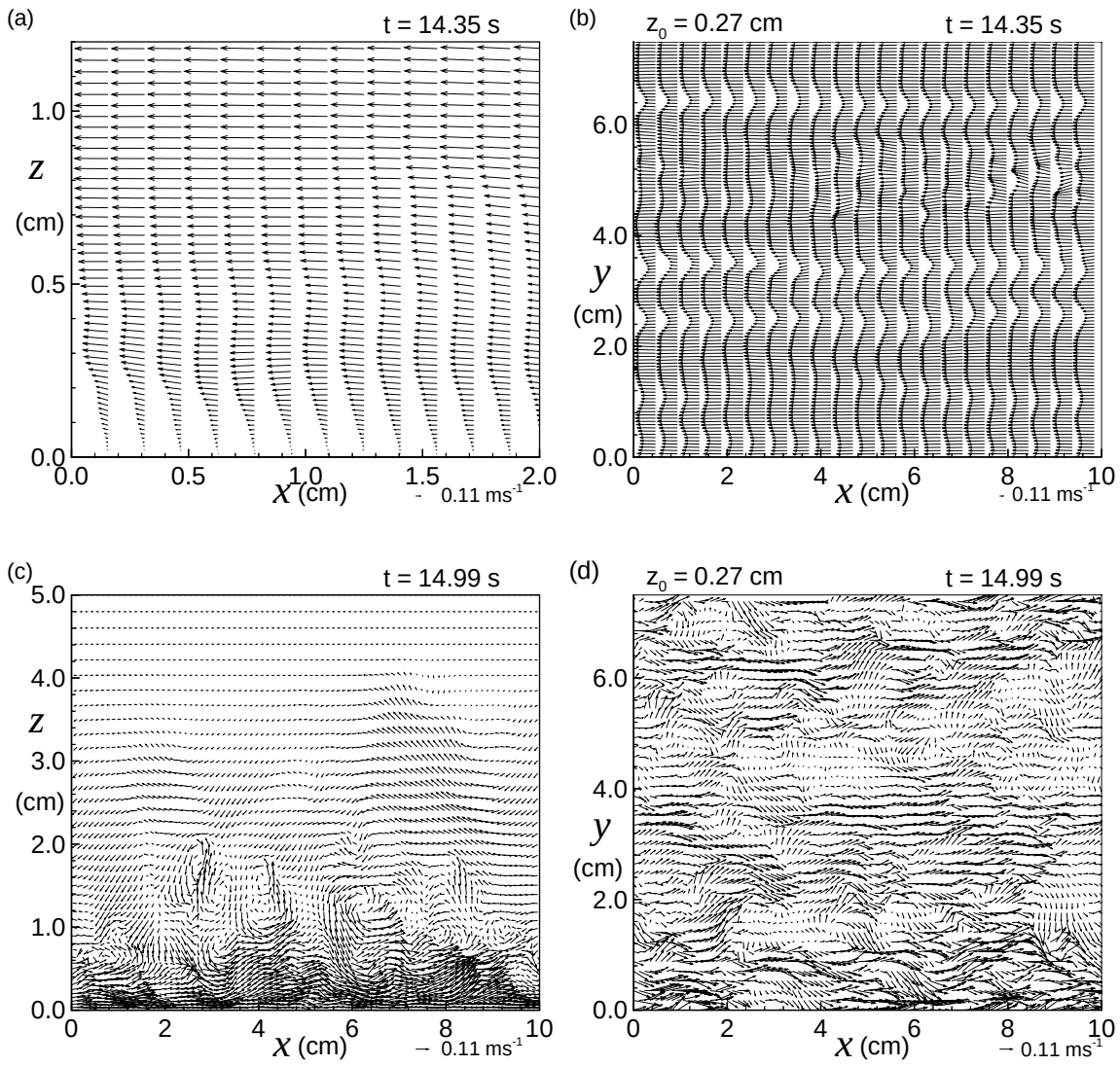

Figure 4: Two-dimensional cross sections of velocity vectors during flow deceleration at (a) and (b), $t = 14.35$ s, and during flow reversal at (c) and (d), $t = 14.99$ s, in side views (a) and (c), $y_0 = 3.75$ cm, and top views (b) and (d), $z_0 = 0.27$ cm.

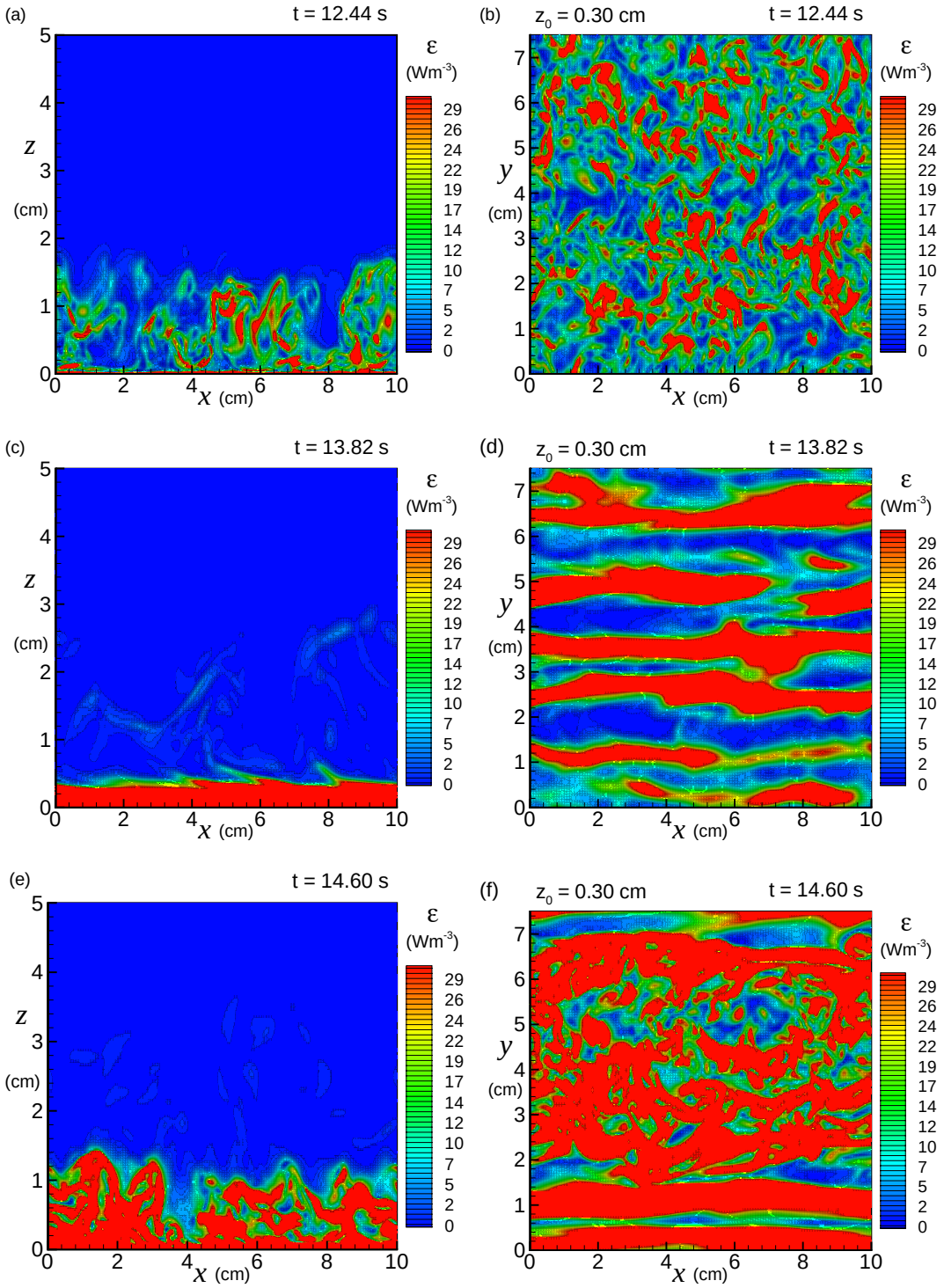

Figure 5: Kinetic energy dissipation rate contours in the boundary layer for Case 1 in the x-z plane at $y_0 = 3.75$ cm, side view panels (a), (c), and (e), and in the x-y plane at $z_0 = 0.30$ cm, top view panels (b), (d), and (f), at different phases of the wave cycle: (a) and (b), $t = 12.44$ s; (c) and (d), $t = 13.82$ s; (e) and (f), $t = 14.60$ s.

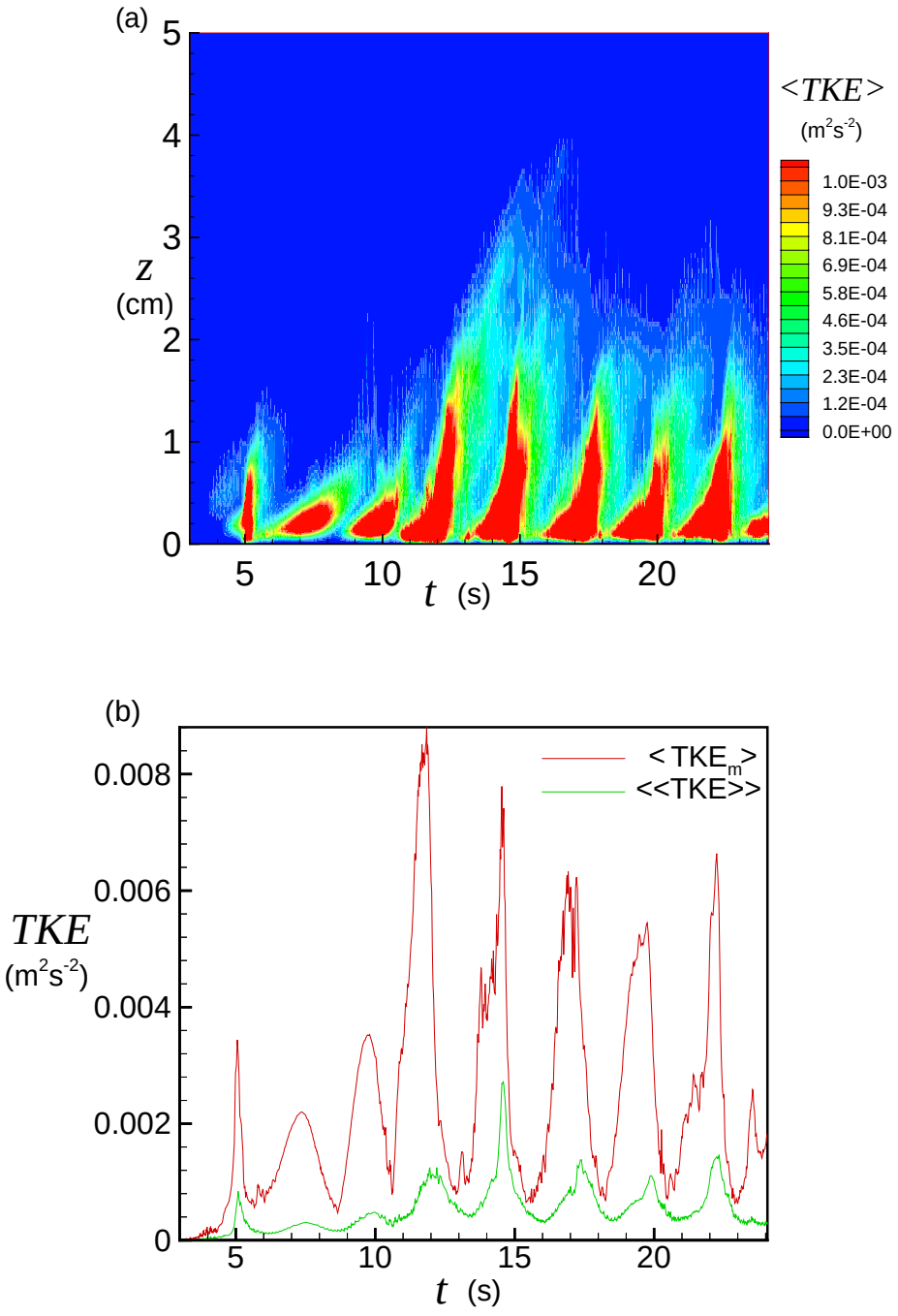

Figure 6: Horizontally averaged turbulent kinetic energy $\langle TKE(z,t)\rangle$ (m^2 s^{-2}) (a) for a five-second period sine wave of maximum amplitude 0.80 m s^{-1} (Case 1) and volume averaged (b) $\langle\langle TKE(t)\rangle\rangle$ and local maximum horizontally averaged turbulent kinetic energy $\langle TKE_m(t)\rangle$.

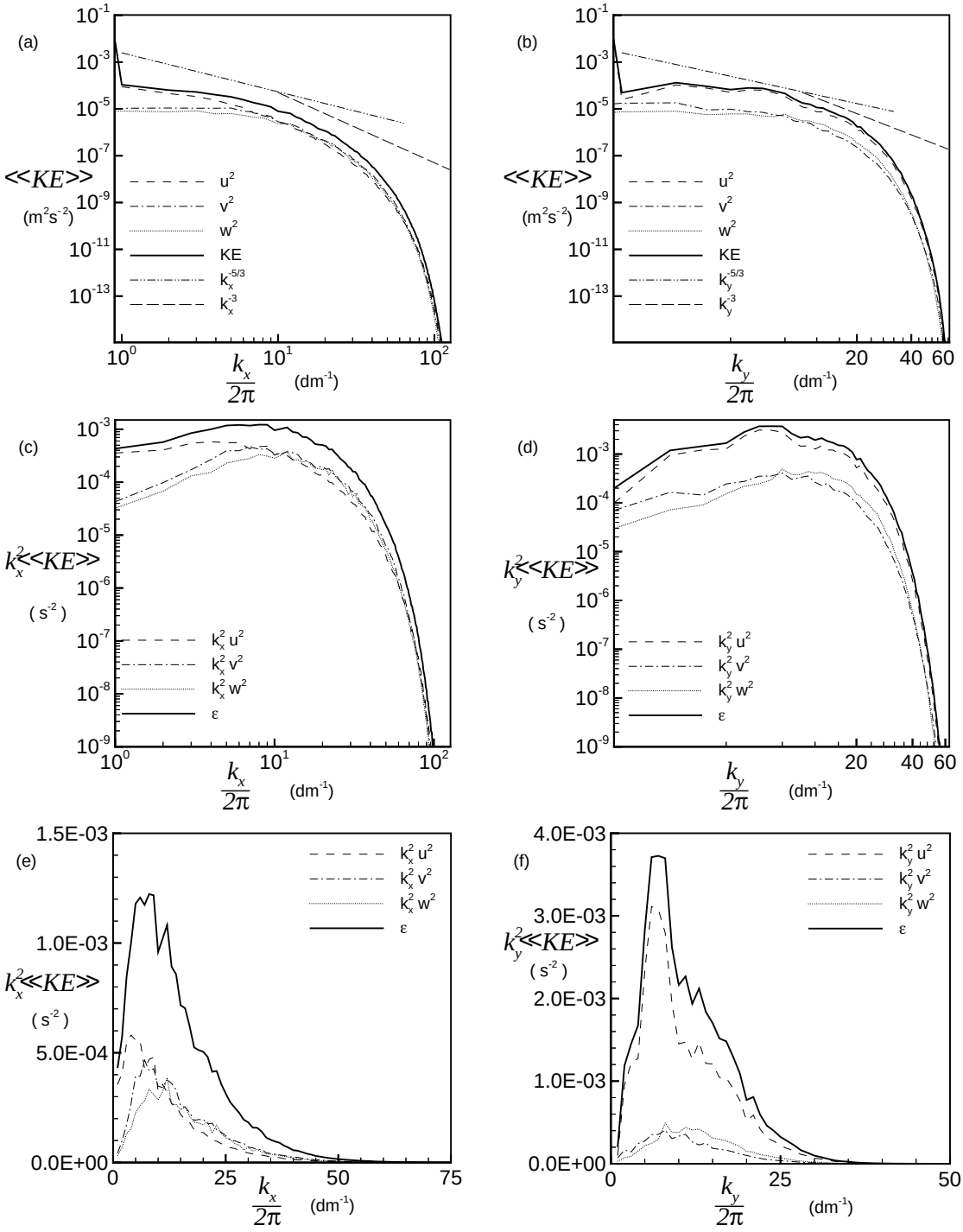

Figure 7: Volume averaged kinetic energy spectra decomposed in (a) the x-direction; (b) the y-direction; kinetic energy dissipation rate spectra in standard log-log form decomposed in (c) the x-direction and (d) the y-direction; and kinetic energy dissipation rate spectra in linear form decomposed in (e) the x-direction and (f) the y-direction for Case 1 at $t = 12.0$ s.

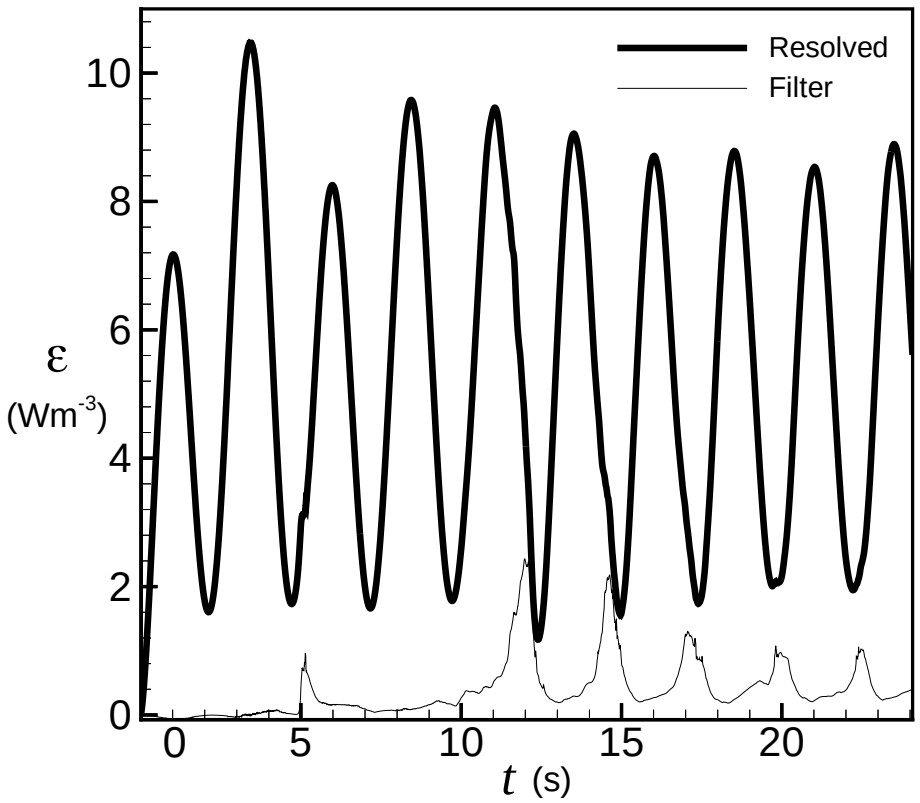

Figure 8: Volume averaged kinetic energy dissipation rates measured from the numerical experiments at well resolved scales ($Resolved$) and from the subgrid scale filter ($Filter$).

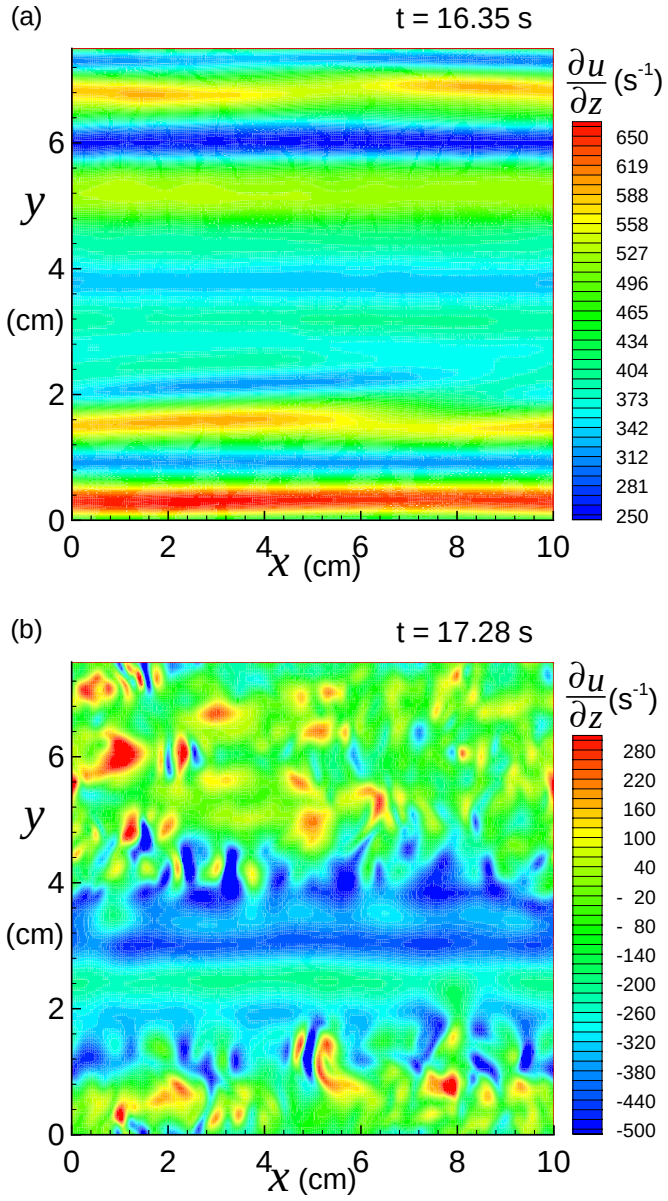

Figure 9: Wall shear component $\left.\frac{\partial u}{\partial z}\right|_w$ in an x-y plane for Case 1, $T = 5$ s, near maximum flow at (a) $t = 16.35$ s, and near flow reversal at (b) $t = 17.28$ s.

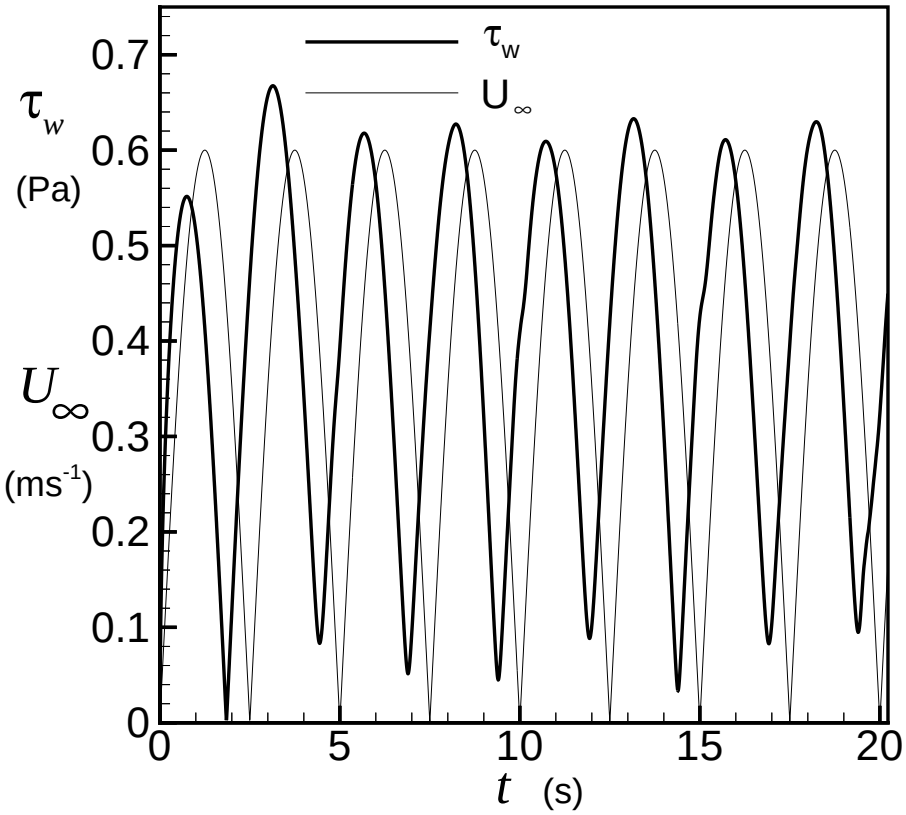

Figure 10: Comparison of the root mean squared wall shear component $\tau_w = \mu\langle\frac{\partial u}{\partial z}|_w\rangle$ and absolute value of the free stream velocity $|U_\infty|$ as a function of time.

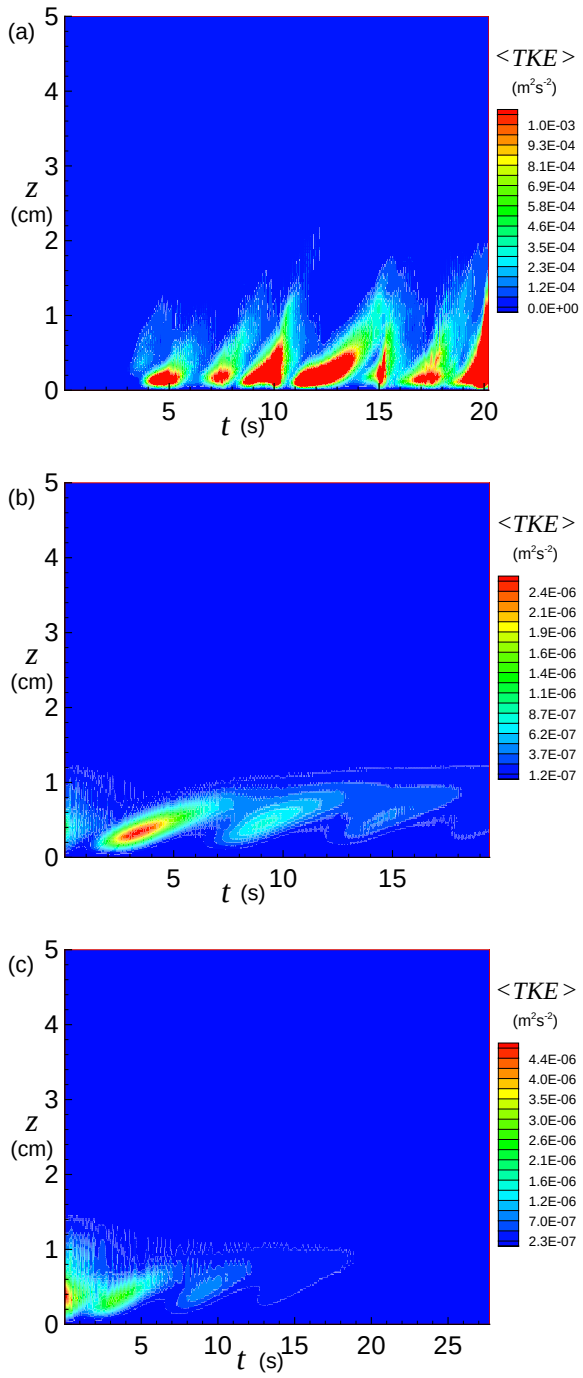

Figure 11: Horizontally averaged turbulent kinetic energy $\langle TKE(z,t)\rangle$ (m^2 s^{-2}) for (a) Case 2, $U_m = 0.6$ m s^{-1}; (b) Case 3, $U_m = 0.4$ m s^{-1}; and (c) Case 4, $U_m = 0.2$ m s^{-1}; compare also to Figure 6 (a) for Case 1, $U_m = 0.8$ m s^{-1}; note change of scale in contour legend for each panel.

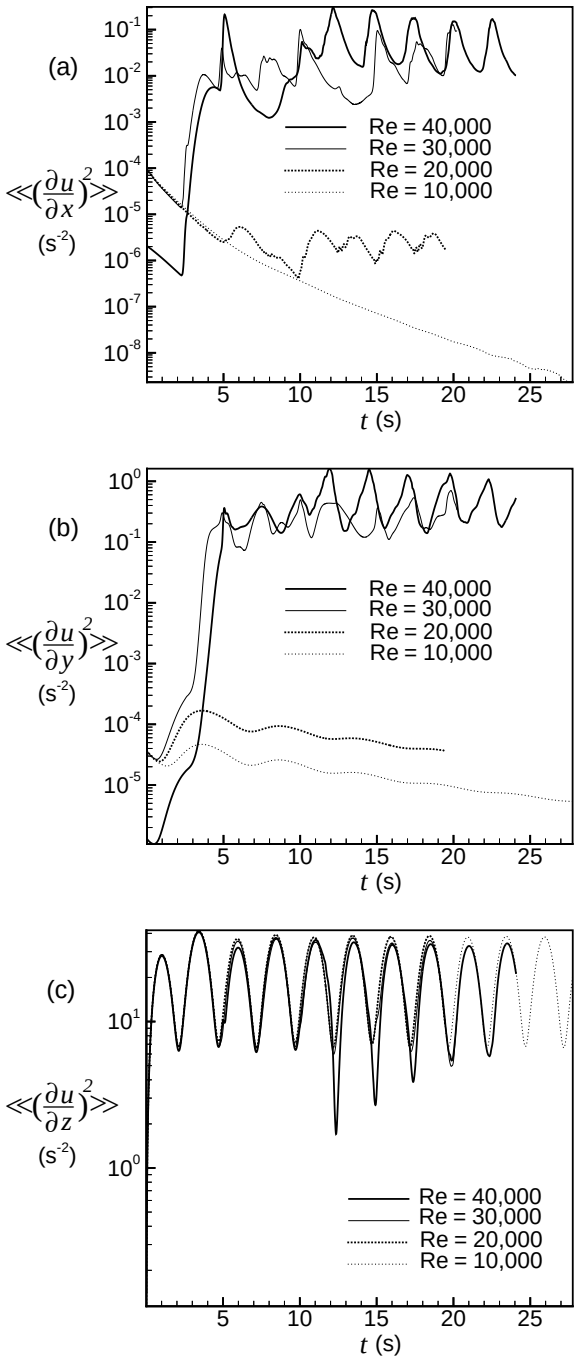

Figure 12: Volume mean square shear as a function of time for (a) $\left\langle\left\langle \frac{\partial u}{\partial x}^2 \right\rangle\right\rangle$, (b) $\left\langle\left\langle \frac{\partial u}{\partial y}^2 \right\rangle\right\rangle$, and (c) $\left\langle\left\langle \frac{\partial u}{\partial z}^2 \right\rangle\right\rangle$ for Case 1, Re = 40,000; Case 2, Re = 30,000; Case 3, Re = 20,000; and Case 4, Re = 10,000.

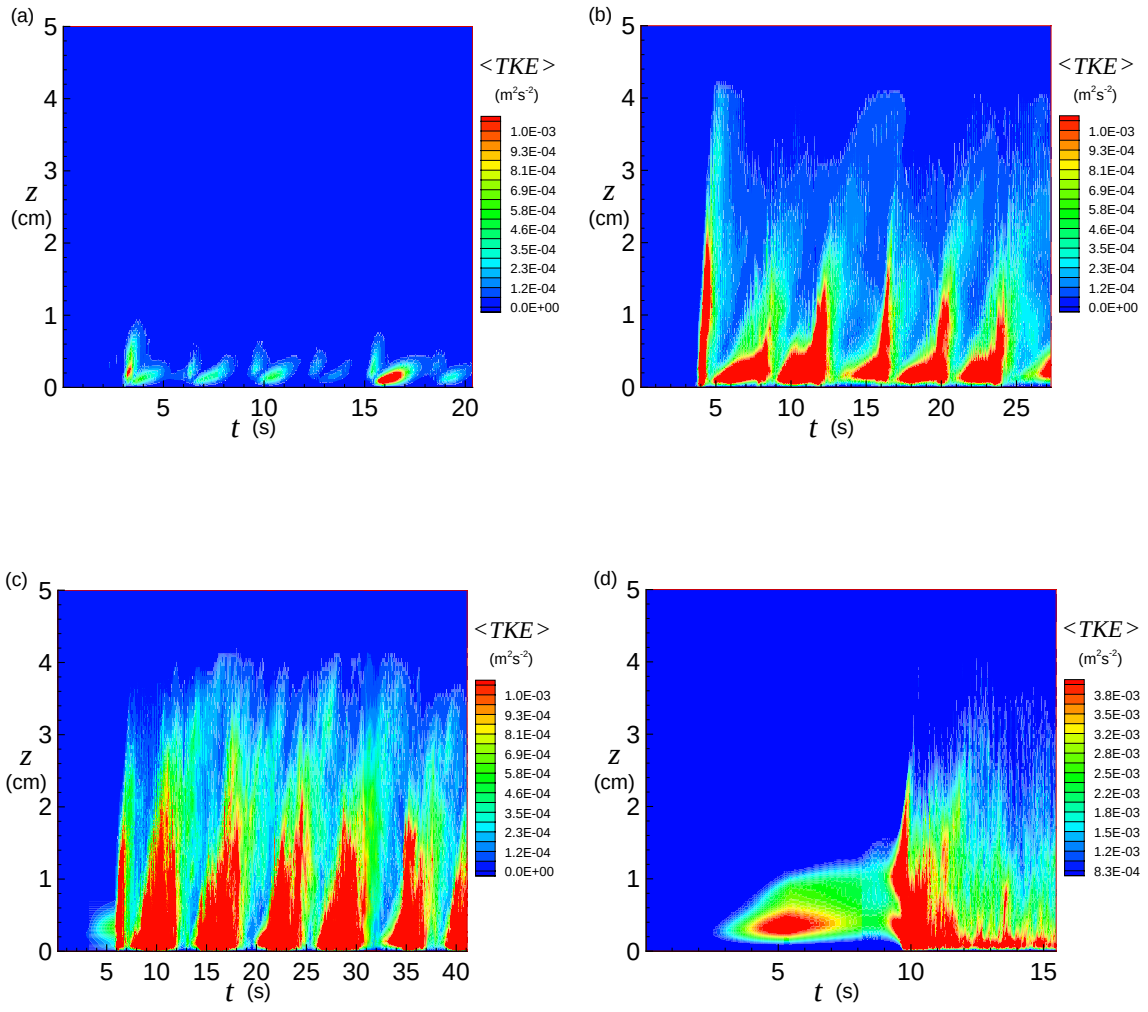

Figure 13: Horizontally averaged turbulent kinetic energy $\langle TKE(z,t)\rangle$ (m^2 s^{-2}) for (a) Case 5, $T = 3$ s; (b) Case 6, $T = 8$ s; (c) Case 7, $T = 12.5$ s; (d) Case 8, $T = \infty$; compare also to Figure 6 (a) for Case 1, $T = 5$ s; note change of scale in contour legend for panel (d).

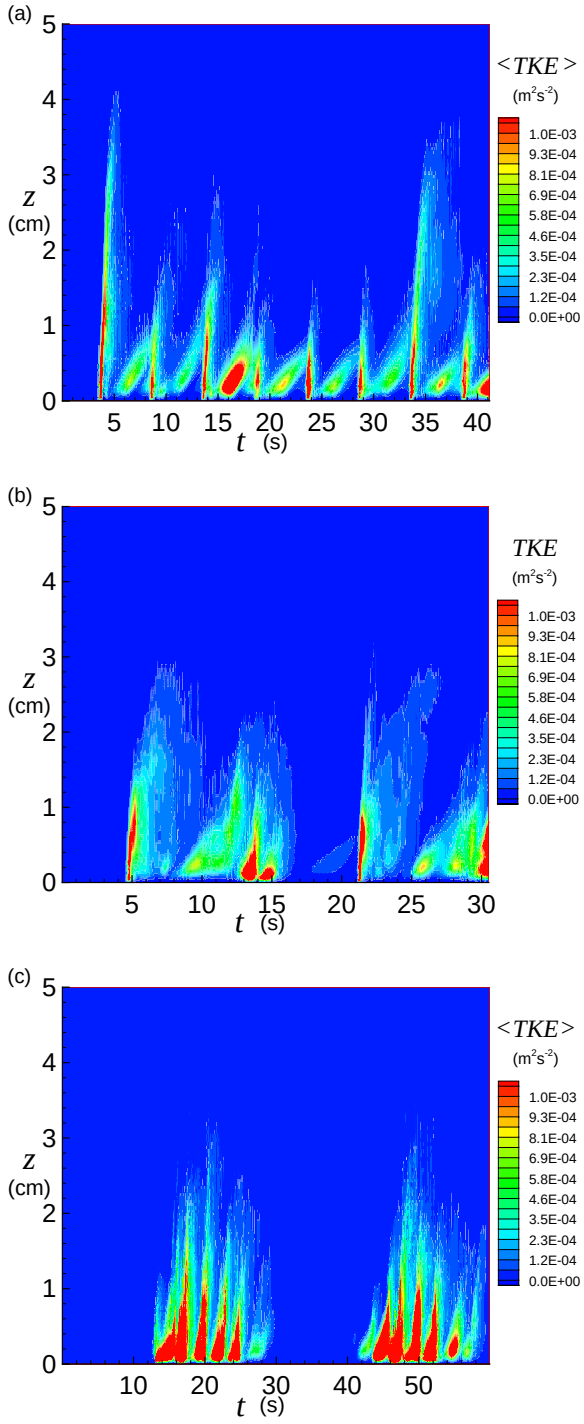

Figure 14: Horizontally averaged turbulent kinetic energy $\langle TKE(z,t)\rangle$ (m^2 s^{-2}) for (a) Case 9, skewed wave; (b) Case 10, complex frequency wave; and (c) Case 11, wave packet.

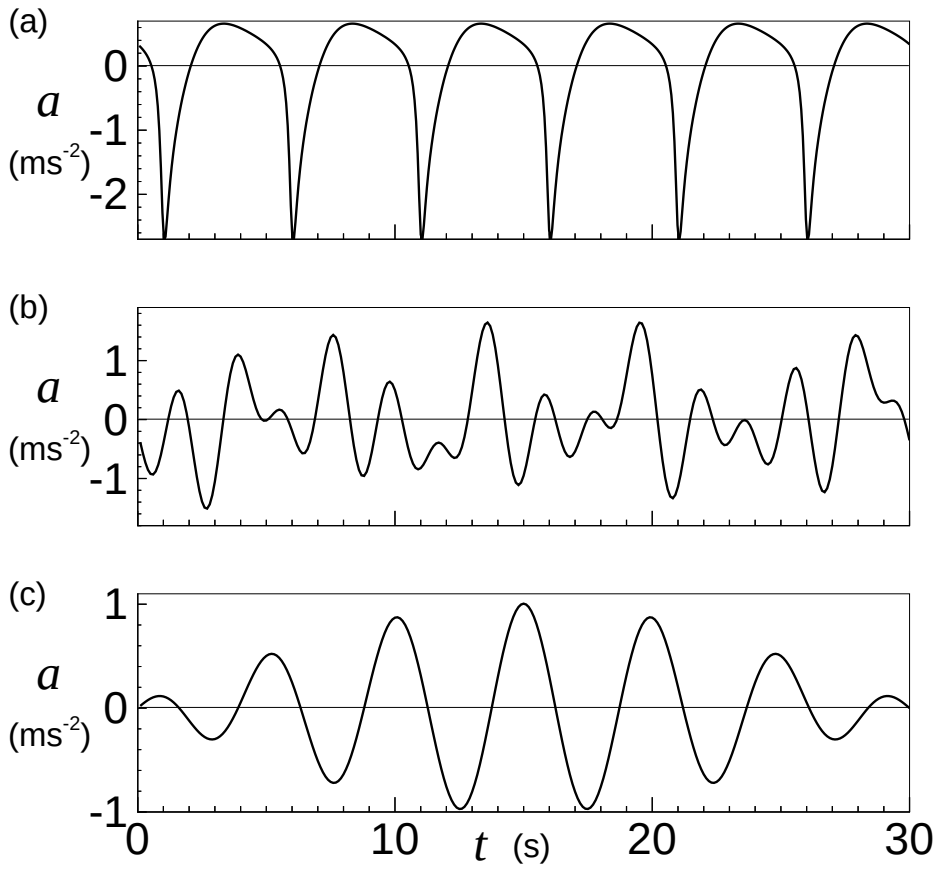

Figure 15: Time derivative of the free stream velocity, $a = \dfrac{\partial U_\infty(t)}{\partial t}$, for different shapes of waves (a) Case 9, skewed wave; (b) Case 10, complex wave; and (c) Case 11, wave packet.

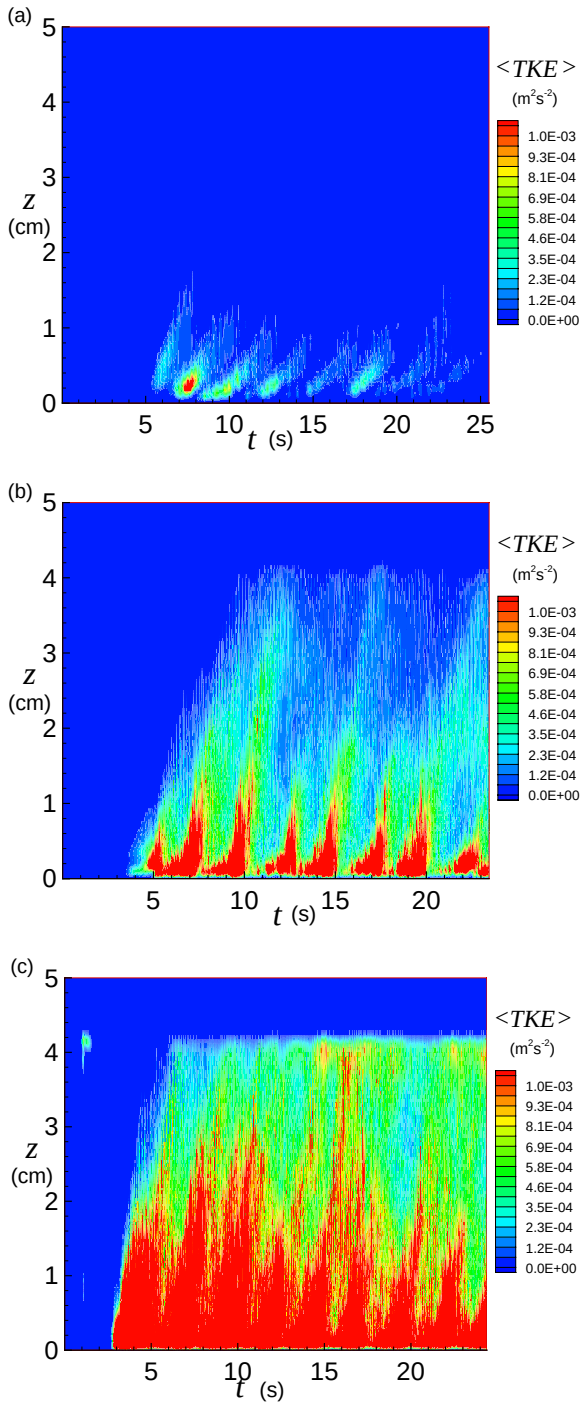

Figure 16: Horizontally averaged turbulent kinetic energy $\langle TKE(z,t)\rangle$ (m^2 s^{-2}) for a sine wave, $T = 5$ s and $U_m = 0.60$ m s^{-1} and a mean current (a) Case 12, $V_\infty = 0.15$ m s^{-1}; (b) Case 13, $V_\infty = 0.30$ m s^{-1}; and (c) Case 14, $V_\infty = 0.60$ m s^{-1}; compare also to Figure 11 (a) for Case 2, $V_\infty = 0.0$ m s^{-1}.

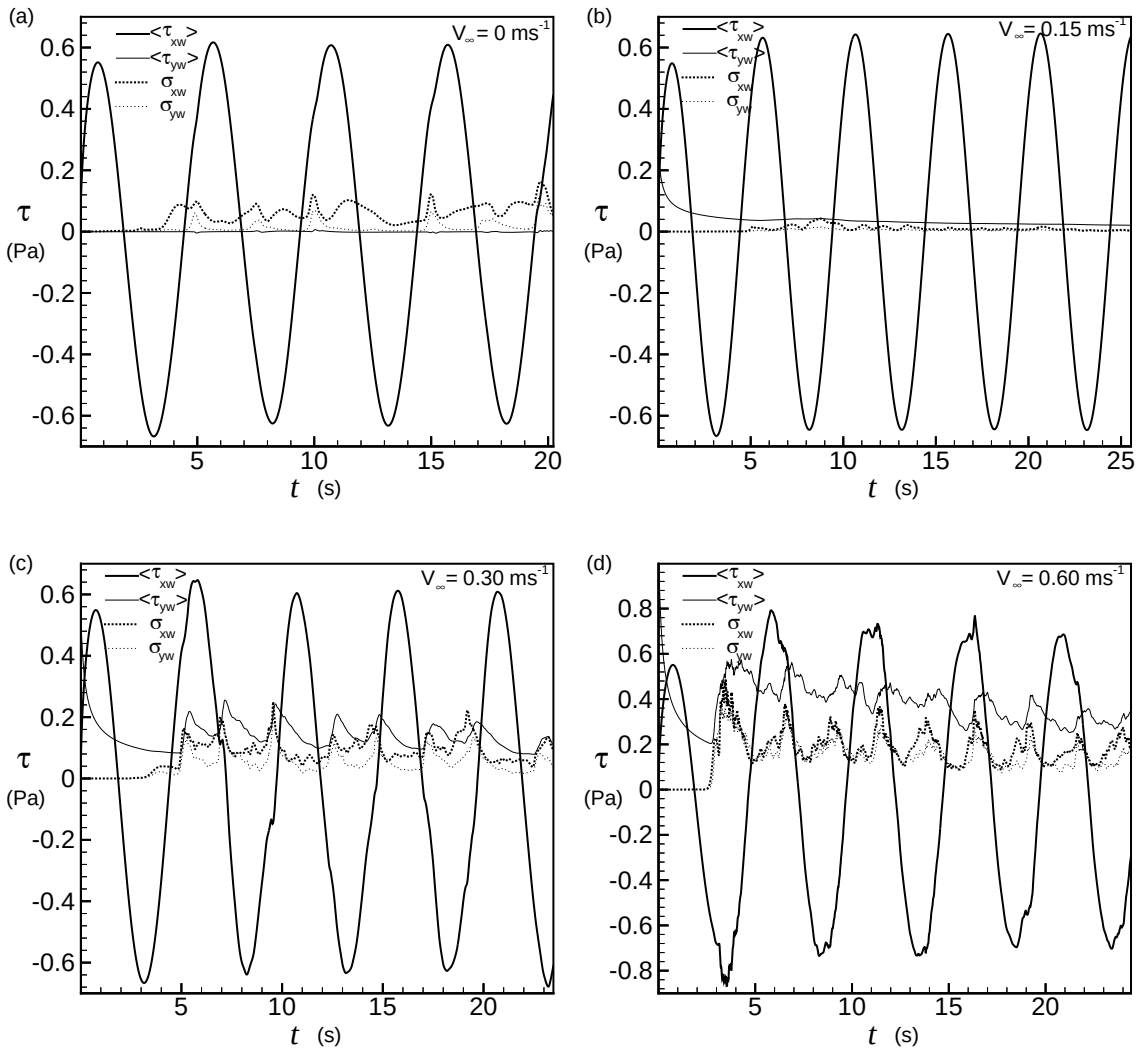

Figure 17: Horizontally averaged wall shear components $\langle \tau_{xw} \rangle = \mu \left\langle \left. \frac{\partial u}{\partial z} \right|_w \right\rangle$ and $\langle \tau_{xw} \rangle = \mu \left\langle \left. \frac{\partial v}{\partial z} \right|_w \right\rangle$ (Pa) and root mean squared (rms) variance σ_{xw} and σ_{yw} (Pa), e.g., $\sigma_{xw} = \mu \left\langle \left(\left. \frac{\partial u}{\partial z} \right|_w (x,y,t) - \left\langle \left. \frac{\partial u}{\partial z} \right|_w (t) \right\rangle \right)^2 \right\rangle^{1/2}$, for different cases of wave-mean current flow: (a) Case 2, $V_\infty = 0.0$ m s^{-1}; (b) Case 12, $V_\infty = 0.15$ m s^{-1}; (c) Case 13, $V_\infty = 0.30$ m s^{-1}; and (d) Case 14, $V_\infty = 0.60$ m s^{-1}, all with $U_\infty(t) = 0.6 \sin(\frac{2\pi}{5} t)$ m s^{-1}.

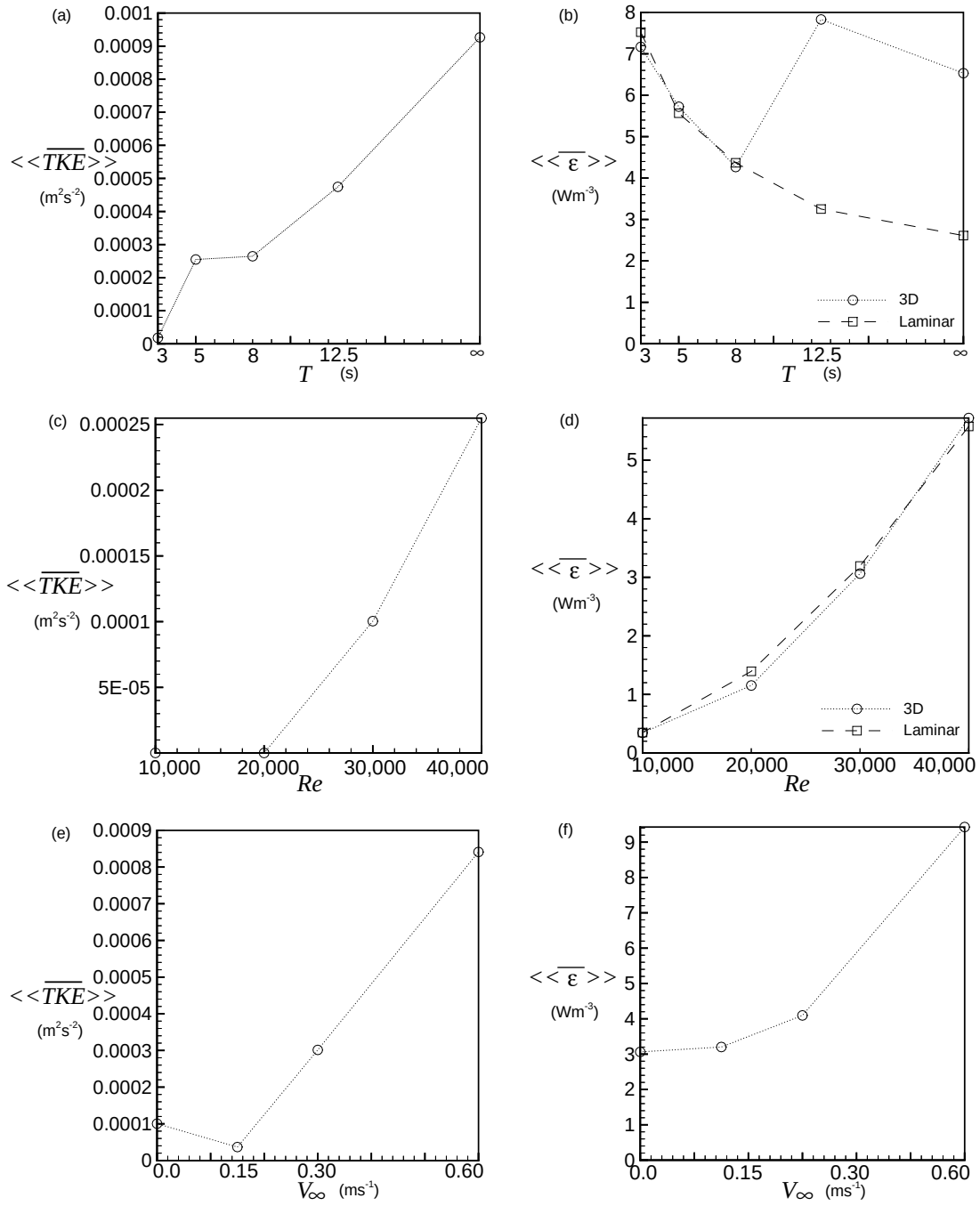

Figure 18: Spatial and temporal mean of turbulent kinetic energy for various experiments with (a) different values of the wave period T; (c) different Reynolds numbers with $T = 5$ s; and (e) different values of current V_∞. Spatial and temporal mean of kinetic energy dissipation rate from the turbulent simulations compared to laminar results for (b) different values of the wave period T; (d) different Reynolds numbers with $T = 5$ s; and (f) different values of current V_∞.

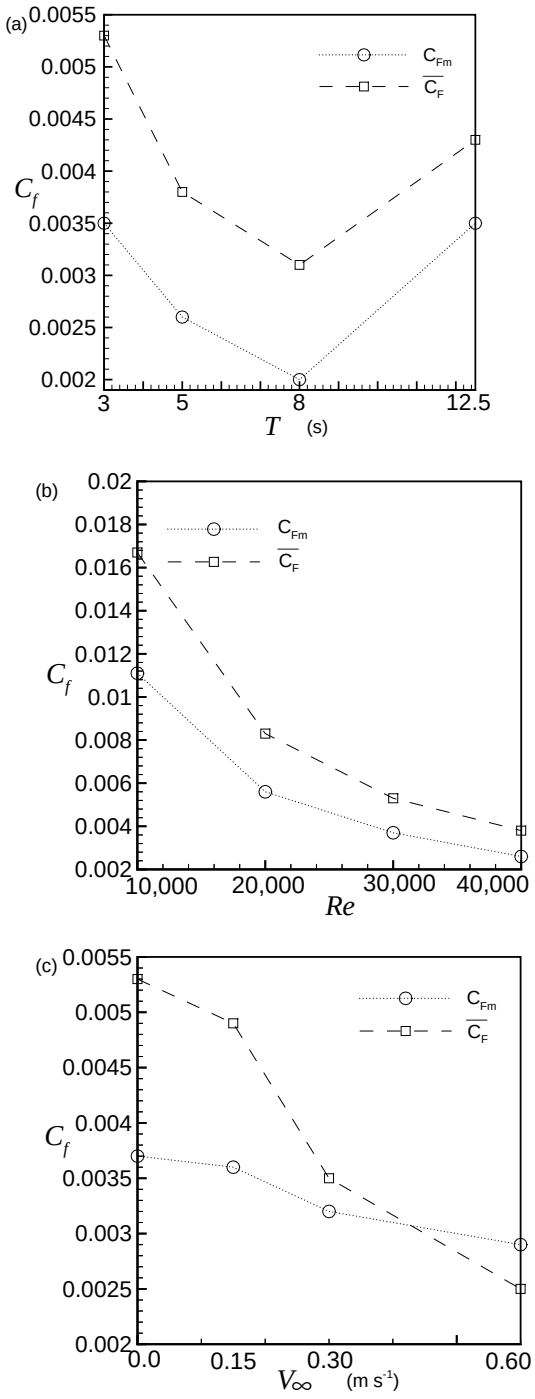

Figure 19: Friction coefficients, C_{fm}, based on maximum values of the horizontally averaged wall shear and velocity amplitude; and $\overline{C_f}$ based on time average values of the horizontally averaged wall shear and the mean velocity amplitude; for various experiments with (a) different values of the wave period T; (b) different Reynolds numbers with $T = 5$ s; and (c) different values of mean current V_∞.